Supporting Information

Carborane-thiol Protected Propeller-Shaped Photoresponsive Silver Nanomolecule

Arijit Jana,[a] Parvathy M. Unnikrishnan,[a] Ajay K. Poonia,[b] Jayoti Roy,[a] Madhuri Jash,[a] Ganesan Paramasivam,[a] Jan Machacek,[c] Kumaran Nair Valsala Devi Adarsh,[b]* Tomas Base[c]* and Thalappil Pradeep[a]*

[a] DST Unit of Nanoscience (DST UNS) and Thematic Unit of Excellence (TUE), Department of Chemistry, Indian Institute of Technology Madras, Chennai – 600036, India

[b] Department of Physics, Indian Institute of Science Education and Research Bhopal, Bhopal – 462066, India

[c] Department of Synthesis, Institute of Inorganic Chemistry, The Czech Academy of Science, 1001 Husinec - Rez, 25068, Czech Republic

Email:

*T.P.- pradeep.iitm.ac.in

*T.B. - tbase@iic.acs.cz

*K.N.V.D.A. - adarsh@iiserb.ac.in

Table of Contents

1. Experimental Procedures Chemicals

Silver nitrate ($AgNO_3$) was purchased from Rankem Chemicals. Triphenylphosphine and sodium borohydride ($NaBH_4$, 98%) were bought from Aldrich. The *meta*-carborane 9-thiol (MCT) ligands were purchased from Katchem s.r.o. (Czech Republic). MCT ligand was re-crystallized from hot chloroform/hexane solvents. Milli-Q water was used for Ag_{18} synthesis and its purification. Deuterated chloroform ($CDCl_3$, 99.8 atom % D) was received from Sigma-Aldrich. HPLC-grade solvents such as methanol, ethanol, acetone, dichloromethane (DCM), chloroform, 1, 2-dichlorobenzene (DCB), dimethylsulfoxide (DMSO) and dimethylformamide (DMF) were purchased from Rankem chemicals. All the chemicals are commercially available and used as such without any purification.

Synthesis of $[Ag_{18}(TPP)_{10}H_{16}]$ nanocluster

The $[Ag_{18}(TPP)_{10}H_{16}]$ nanocluster was synthesized by following a reported procedure.[1, 2] Briefly, 20 mg of $AgNO_3$ was dissolved in 5 ml methanol and 7 ml of chloroform was added to it. After that, 70 mg of triphenylphosphine dissolved in 2 ml of chloroform was added to the above reaction mixture under vigorous stirring conditions. After 20 min, 6.5 mg sodium borohydride dissolved in 0.75 ml of mill-Q water was added. Upon addition of the reducing agents, the colorless solution becomes yellow. The reaction was continued for 3.5 h. in dark condition. During the progress of the reaction, the color of the solution changes to brownish black and finally dark green, which indicate the formation of the nanocluster. Mixed solvents were removed by evaporation under reduced pressure. The solid green material was washed repeatedly to remove the excess reagents. The Ag_{18} nanocluster was characterized using UV-vis absorption spectroscopy and mass spectrometric studies (shown in Figure S1). Purified nanocluster was extracted in methanol and used for Ag_{21} synthesis. The yield of the product was 35% in terms of silver.

Synthesis of $[Ag_{21}(MCT)_{12}(TPP)_2]$ nanocluster

The Ag_{21} nanocluster was prepared using the LEIST reaction of Ag_{18} nanocluster with MCT ligands. In brief, 8 mg of MCT ligands are added to a solution having 10 mg of Ag_{18} nanocluster in 5 ml methanol. After 10 min of the addition of thiol, the solution became yellowish and which eventually converted to dark red. After 2 hours of reaction, a dark reddish solution forms as an end product. After overnight size focusing, centrifugation of the reaction mixture ends up a reddish precipitate, which was extracted in DCM after the multiple cleaning of methanol. As prepared Ag_{21} nanoclusters are insoluble in methanol but soluble in DCM, chloroform and DMF. Suitable quality single crystals are grown following the vapor diffusion of hexane into a concentrated cluster solution in DCM. The yield of the product is 65% in terms of Ag_{18} nanocluster. As formed Ag_{21} nanocluster with twelve MCT and two TPP ligands is the predominant product during this LEIST reaction. There are no other cluster products during this synthetic reaction.

Effect of heating

The thermal stability of Ag_{21} crystals was measured in ambient conditions after preparing a thin film of 8-10 mg microcrystalline powder. After 4 h of heating, we have measured Raman spectra as such and UV-vis spectra were recorded upon dissolving it in DCM. Figures 6d and 6e represent the combined results after each heating.

Effect of light-illumination

The effect of photo-illumination of Ag_{21} crystals was measured in the solid state under ambient conditions. A white light source (Xe arc lamp) with varying lamp power of 50-200 W was used for the illumination. Light was exposed to the sample vertically using an optical light guide. After 4 h of light exposure, we have

measured the Raman spectra as such and UV-vis absorption spectra were recorded upon dissolving the sample in DCM. Figures 6g and 6h show the combined results after each light exposure.

2. Instrumentation

Spectroscopic characterization

UV-vis absorption spectra were measured using Perkin Elmer Lambda 365 UV-Vis spectrophotometer in the wavelength region of 200 to 1100 nm with a bandpass filter of 1 nm. 20 mM purified cluster (in 2.5 ml of respective solvents) was used for the measurements. Mass spectra of all the nanoclusters were measured using the Waters Synapt G2 Si HDMS instrument. This mass spectrometer consists of an electrospray ionization source, quadrupole ion guide/trap, ion mobility cell and TOF analyzer. Nitrogen gas was used as the nebulizer gas. The mass spectra were collected in positive ion-mode. Mass spectrometric measurements were done by using the following conditions: Flow rate: 20 μL/min, capillary voltage: 2.5 kV, cone voltage: 20 V, source temperature: 80 °C, desolvation temp: 150 °C, desolvation gas flow: 400 L/h. All the fragmentation experiments were performed by varying the collision energy of the selected ions inside the ion mobility cell using the same instrument. Circular dichroism (CD) spectra were recorded using an Applied Photophysics instrument having Chirascan software. 20 mM cluster dissolved in 2.5 ml DCM was used for the measurement. Photoluminescence spectra were measured using Jobin Yvon Nanolog fluorescence spectrometer with a bandpass of 3 nm for both emission and excitation spectra. FT-IR spectra were recorded using JASCO-4100 spectrometer. 1 mg crystals were finely grinded with dry KBr to prepare a thin pallet for the measurement. Multinuclear NMR spectra were recorded using Bruker 500 MHz FT-NMR spectrometer. Deuterated chloroform ($CDCl_3$) was used for the measurements. Spectra were processed using MestRe-Nova NMR software. Powder XRD of the Ag_{21} nanocluster was measured using a D8 Advance Bruker instrument, using Cu Kα as an X-ray source (hγ = 8047.8 eV). 150 mg microcrystalline solids were spotted on a clean glass slide for the measurement. A high speed wide angle LYNXEYE detector was used for collecting the data. X-ray photoelectron spectroscopy was measured using ESCA probe TPD equipped with polychromatic Mg Kα X-ray source (hγ = 1253.6 eV). Samples dissolved in DCM were spotted on a sample stub and measurements were conducted with a constant analyzer energy of 50 eV for the survey scans and 20 eV for the specific regions. The binding energies in the spectra were calibrated with respect to the C 1s peak at 284.8 eV. Raman spectra were recorded using a CRM-Alpha 300S, WI Tec GmbH confocal Raman microscope, equipped with 532 nm frequency doubled Nd-YAG laser.

Microscopic characterization

Optical microscopic images of the crystals were collected in reflected light mode using Keyence VHX-950F digital microscope. Scanning electron microscopy (SEM) was performed using Verios G4 UC, Thermo Scientific field emission scanning electron microscope (FESEM). The images were collected in high vacumn at an operating voltage at 2 kV. Transmission electron microscopy (TEM) was measured using a JEOL-3010, 300 kV instrument. A Gatan 794 multiscan CCD camera was used for image collection. The accelerating voltage was kept low to reduce beam-induced damage.

TGA, DTG and DSC measurements

TGA, DTG, and DSC measurements in the temperature range of 25 to 800 °C were measured using a NETZSCH STA 449 F3 Jupiter instrument equipped with Proteus-6.1.0 software. About 8.7 mg crystalline sample was loaded in an alumina crucible for the measurement. Nitrogen was used as the environment with a flow rate of 10 °C/min. Low temperature DSC measurement was performed using NETZSCH 204F1

Phoenix instrument equipped with Proteus 80 software. About 3.22 mg crystalline sample was loaded in an alumina crucible for the measurement in nitrogen gas (flow rate of 60.0 ml/min). DSC data were measured for a cooling cycle from 25 to -90 °C, followed by a heating cycle from -90 to 200 °C.

Femtosecond (fs) transient absorption spectroscopy

In our transient absorption spectrometer, 120 fs pulses centered at 800 nm are generated by Spectra physics Mai-Tai oscillator. The pulsed profile of the laser sources used in our experiment is Gaussian pulse with full width at half maximum (FWHM) of ~ 30 meV. This pulse is send to Spectra physics Spitfire amplifier to generate high energy (4mJ/pulse) with a repetition rate of 1 KHz. To generate 400 nm pump pulse, one part of the beam is incident on the second harmonic β-barium borate crystal and output is separated from the fundamental beam with the help of a dichroic beam splitter. The residual 800 nm pulses are delayed with respect to the pump by a computer-controlled motion controller and pass through a CaF_2 crystal to generate the white light continuum probe beam. Here to avoid any photodamage, the crystal is continuously rotated throughout the experiment. Now both the pump and probe pulses are spatially overlapped onto the sample and the changes of absorbance (ΔA) of probe beam due to the pump is calculated using the equation -

$$\Delta A = \log\left[I_{ex}(s)/I_0(s)\right] - \left[I_{ex}(r)/I_0(r)\right]$$

Where *r* and *s* correspond to the reference and sample, I_{ex} and I_o are transmitted intensities of probe pulse after excitation and in the ground state, respectively. The intensity of transmitted pulses is measured with the help of MS 2004 (600 lines/mm diffraction grating blazed at 600 nm) spectrometer and Si linear photodiode arrays. The TA data is chirped corrected before analyzing to compensate for the group velocity dispersion. The magnitude of the chirp is measured by using the instantaneous coherent artefact response of the ethanol solution. The measurements are carried out inside the motorized sample holder where it is continuously rotated during the experiment.

Nanosecond (ns) flash photolysis

The ns transient absorption is measured using flash photolysis. In these measurements, we excite the sample using the second harmonic of Nd-YAG laser pump having the pulse width of 5 ns (< 10 meV) centred at 532 nm of Spectra Physics Quanta-Ray INDI laser system. The change in absorbance is determined by the white light (500-800 nm), which is produced using Xenon-Arc lamp (150 W). In the set-up, obtained probe beam is aligned in the cross beam configuration to the pump laser beam. The ns flash photolysis measurement is performed in a quartz cuvette. The change in the intensity is measured by Laser flash photolysis spectrometer (LKS80Applied Photophysics) with the combination of an oscilloscope (Agilent Infiniium DSO9064A).

Single crystal XRD measurements

Single-crystal X-ray diffraction data were recorded using Bruker D8 VENTURE instrument equipped with Mo Kα radiation source of wavelength 0.71073 Å. A PHOTON 100 CMOS detector has been used to record the diffraction spots. A suitable crystal was mounted on a Kapton loop with the help of paratone oil. The programme APEX3-SAINT (Bruker, 2016) was used for integrating the frames. A multi-scan absorption correction was done using the programme SADABS (Bruker, 2016). The structure was solved by SHELXT-2014 (Sheldrick, 2014) and refined by full-matrix least squares techniques using SHELXL-2018 (Sheldrick, 2018) computer programme. Hydrogen atoms were fixed at calculated positions and refined as riding model

with C-H = 0.93 Å, B-H = 1.10 Å and Uiso(H) = 1.2 Ueq(C) or 1.2 Ueq(B). Mercury 2020.2.0 software has been used for the visualization of the structure.

3. Theoretical calculations

The structural, electronic and optical absorption spectra were calculated using density functional theory (DFT) and time-dependent density functional theory (TD-DFT) as implemented in the Grid-based Projector Augmented Wave (GPAW) software package.[3, 4] The atomic coordinates were taken from the single crystal structure to initiate the structural optimization. The exchange function Pardew-Burke-Ernzerhof (PBE)[5] was used in the real grid space with the spacing of 0.2 Å to understand the optimized geometry. The valence electronic configuration of Ag ($4d^{10}$ $5s^1$ $5p^6$), S ($3s^2$ $3p^4$), P ($3s^2$ $3p^3$), C ($2s^2$ $2p^2$), B ($2s^2$ $2p^1$) and H ($1s^1$) were used for the PAW setup and scalar relativistic effects were included for the Ag atoms. The geometry optimization was carried out with the convergence condition without taking any symmetry constraints with a residual force less than 0.05 eV/Å. The absorption spectrum was calculated using linear response time-dependent density functional theory (LR-TDDFT). The origin of each absorption feature was calculated using the ground state and excited state optimized geometry. The total density of states (DOSs) was calculated for each transition and the involvement of individual atomic orbitals was also analyzed. Visualization of structure and individual molecular orbitals were done with visual molecular dynamics (VMD) software.

Table S1. Crystal data and structure refinement for Ag_{21} nanocluster.

Identification code	Ag_{21} nanocluster	
Empirical formula	$C_{60}\ H_{162}\ Ag_{21}\ B_{120}\ P_2\ S_{12}$	
Formula weight	4893.02	
Temperature	190(2) K	
Wavelength	0.71073 Å	
Crystal system	Cubic	
Space group	P a -3	
Unit cell dimensions	a = 26.7447(17) Å	α = 90°.
	b = 26.7447(17) Å	β = 90°.
	c = 26.7447(17) Å	γ = 90°.
Volume	19130(4) $Å^3$	
Z	4	
Density (calculated)	1.699 Mg/m^3	
Absorption coefficient	2.274 mm^{-1}	
F(000)	9324	
Crystal size	0.500 x 0.400 x 0.350 mm^3	
Theta range for data collection	2.850 to 25.994°.	
Index ranges	-32<=h<=32, -32<=k<=32, -32<=l<=32	
Reflections collected	130622	
Independent reflections	6253 [R(int) = 0.0360]	
Completeness to theta = 25.242°	99.7 %	
Absorption correction	Semi-empirical from equivalents	
Max. and min. transmission	0.7457 and 0.5804	
Refinement method	Full-matrix least-squares on F^2	
Data / restraints / parameters	6253 / 0 / 324	
Goodness-of-fit on F^2	1.172	
Final R indices [I>2sigma(I)]	R1 = 0.0748, wR2 = 0.1444	
R indices (all data)	R1 = 0.0952, wR2 = 0.1599	
Extinction coefficient	n/a	
Largest diff. peak and hole	2.620 and -1.877 $e.Å^{-3}$	

Table S2. Atomic coordinates (X 10^4) and equivalent isotropic displacement parameters (Å^{2}x 10^3) for Ag21-1_sq. U(eq) is defined as one third of the trace of the orthogonalized U^{ij} tensor.

	x	y	z	U(eq)
Ag(1)	29(1)	4493(1)	6731(1)	43(1)
Ag(2)	-595(1)	4902(1)	5856(1)	39(1)
Ag(3)	0	5000	5000	24(1)
Ag(4)	529(1)	4995(1)	5899(1)	37(1)
Ag(5)	1332(1)	3668(1)	6332(1)	45(1)
C(1)	2001(6)	5642(8)	7272(7)	96(6)
C(2)	1153(6)	5616(7)	7865(5)	88(5)
C(3)	-923(5)	6236(5)	7055(5)	55(3)
C(4)	-1462(6)	5787(6)	7762(7)	87(5)
C(5)	2449(4)	3436(4)	7025(4)	37(2)
C(6)	2720(4)	3295(5)	7446(4)	53(3)
C(7)	3177(5)	3513(5)	7541(5)	58(3)
C(8)	3368(5)	3863(6)	7231(6)	73(4)
C(9)	3109(6)	4002(6)	6820(7)	83(5)
C(10)	2655(5)	3794(5)	6714(5)	62(3)
S(1)	-854(1)	4597(1)	6712(1)	39(1)
S(2)	916(1)	4519(1)	6607(1)	42(1)
P(1)	1850(1)	3150(1)	6850(1)	34(1)
B(1)	1217(4)	4949(4)	7054(4)	32(2)
B(2)	1574(5)	4726(7)	7564(6)	60(4)
B(3)	2005(6)	5151(8)	7683(6)	79(6)
B(4)	1481(5)	5537(5)	6873(5)	51(3)
B(5)	1874(5)	5040(7)	7058(5)	62(4)
B(6)	945(4)	5519(4)	7253(4)	41(3)
B(7)	992(5)	5009(5)	7683(4)	46(3)
B(8)	1522(7)	5126(8)	8045(5)	82(6)
B(9)	1788(8)	5702(10)	7880(7)	102(8)
B(10)	1432(6)	5936(6)	7373(5)	63(4)

B(11)	-936(4)	5194(4)	7050(4)	34(2)
B(12)	-505(5)	5417(5)	7518(5)	45(3)
B(13)	-499(5)	6090(5)	7484(6)	58(4)
B(14)	-1187(5)	5737(5)	6758(5)	54(3)
B(15)	-549(4)	5738(4)	6934(5)	40(3)
B(16)	-1545(5)	5422(6)	7219(6)	58(4)
B(17)	-1104(6)	5233(5)	7686(5)	53(3)
B(18)	-862(6)	5773(5)	7932(5)	56(3)
B(19)	-1093(7)	6298(6)	7668(6)	68(4)
B(20)	-1522(5)	6091(6)	7201(7)	63(4)

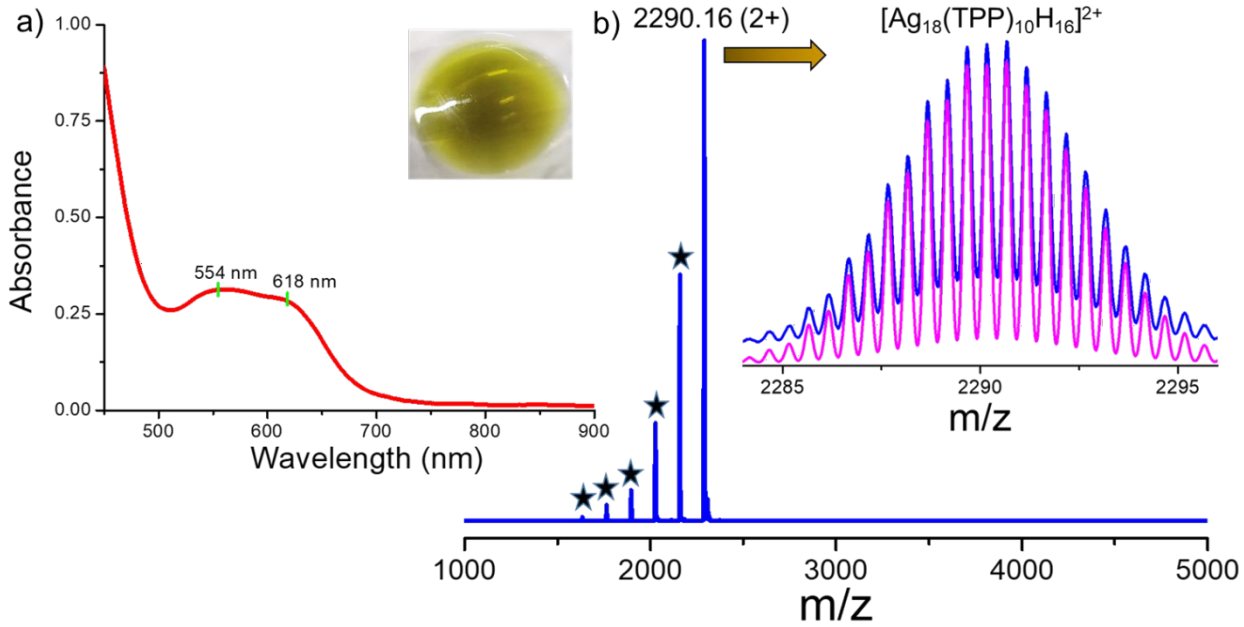

Figure S1. a) UV-vis absorption spectrum of Ag_{18} nanocluster (left inset shows the photographic image of the nanocluster). b) The ESI-MS spectrum of Ag_{18} nanocluster in positive ion mode. Each * indicates sequential loss of TPP units from the parent nanocluster. The right inset shows the exact matching of the experimental spectrum (blue) with the theoretical spectrum (pink).

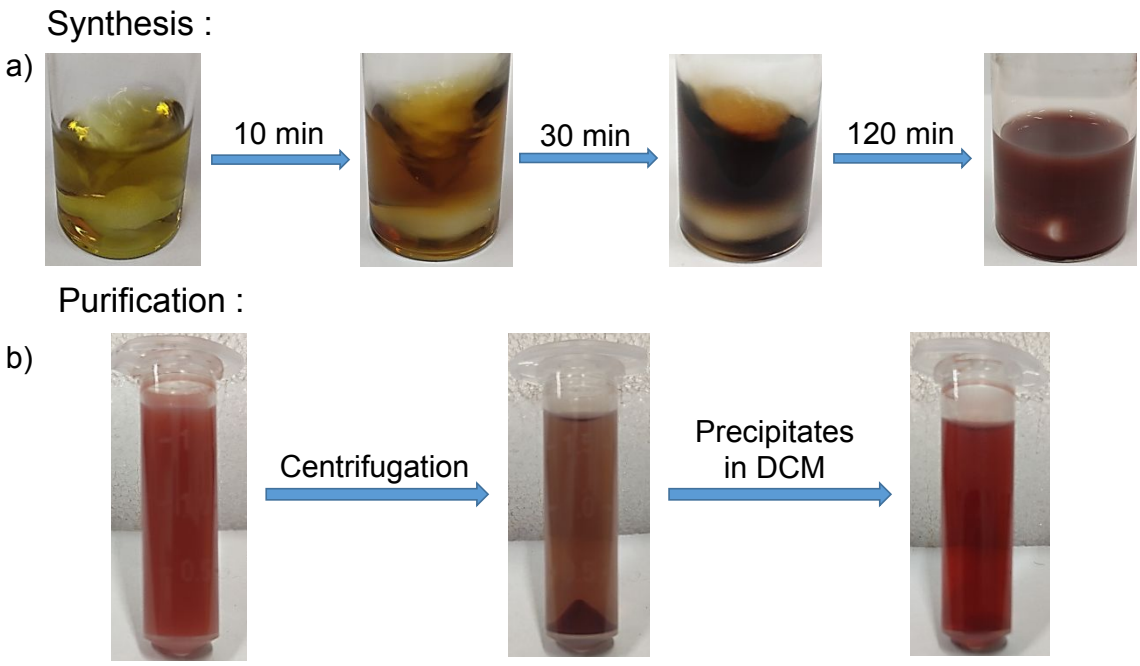

Figure S2. a) Photographic images show the progress of the LEIST reaction. b) Purification of the as synthesized nanoclusters through centrifugation.

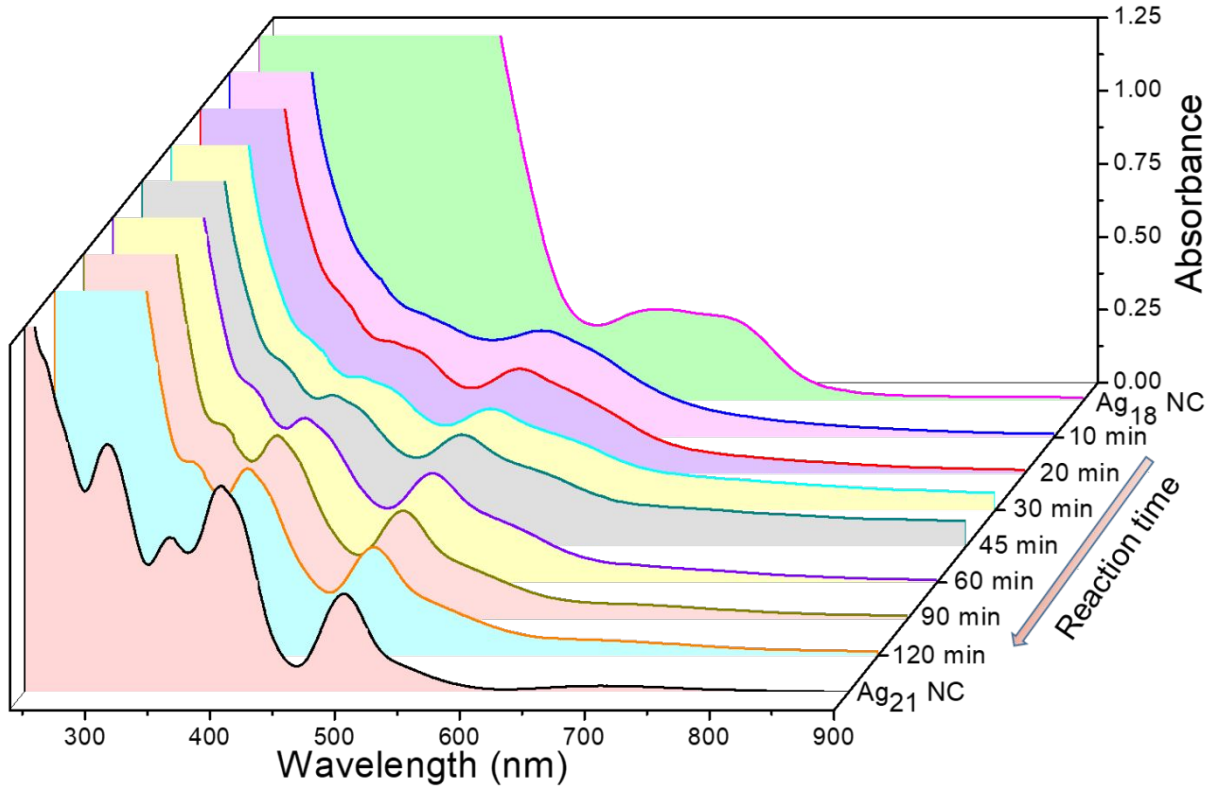

Figure S3. Time-dependent UV-vis absorption spectra show the formation of Ag_{21} from Ag_{18} nanocluster. All of these spectra were measured in methanol.

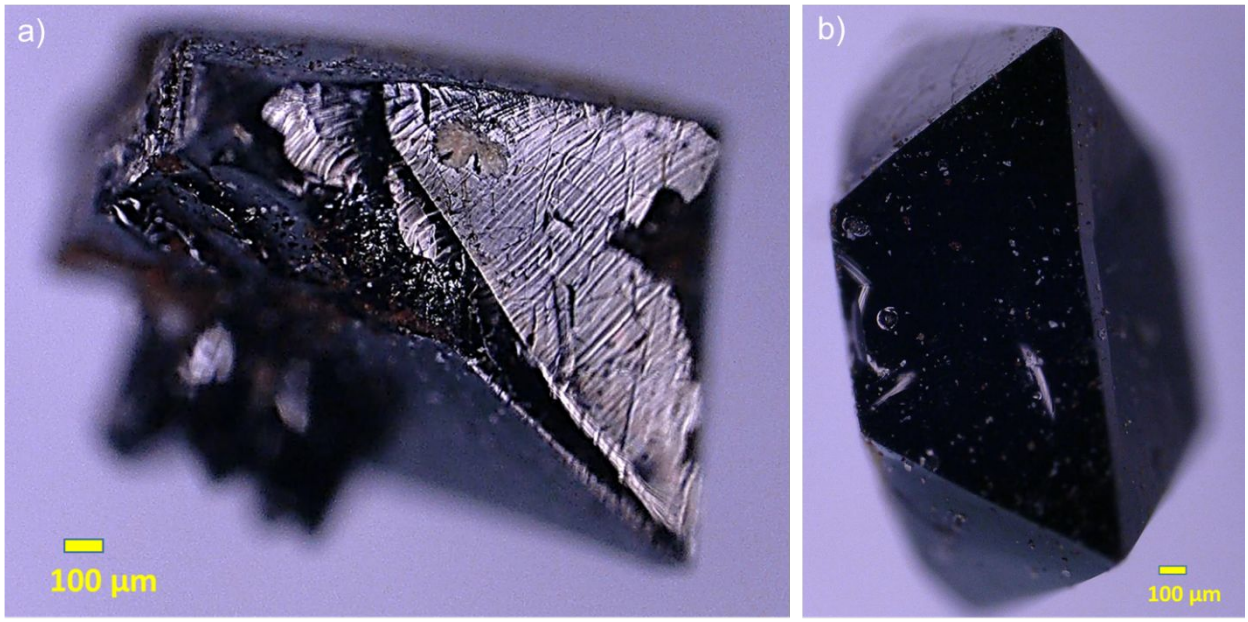

Figure S4. a, b) Optical microscopic images of crystals having pyramidal facets.

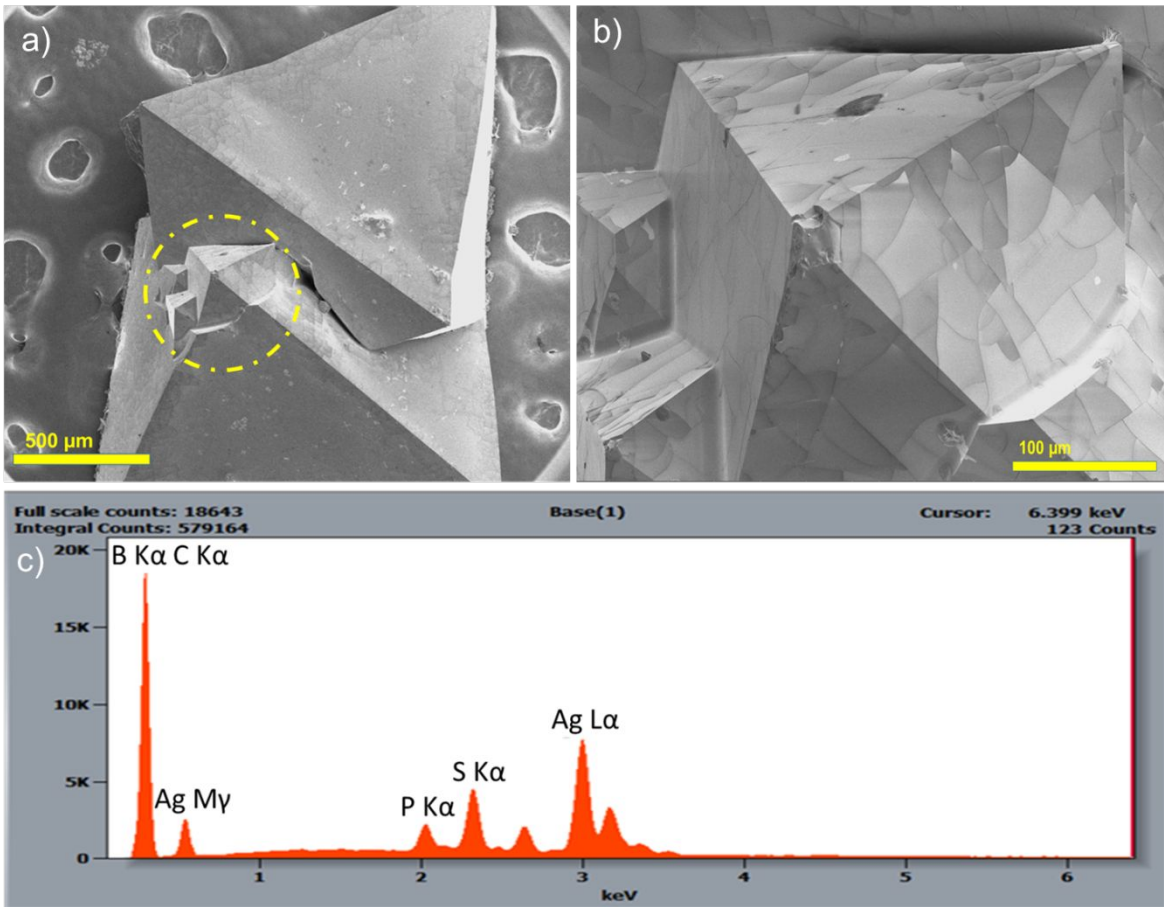

Figure S5. The FESEM microscopic image of a single crystal presenting different crystalline planes, a) lower magnification and b) higher magnification. c) The EDS spectrum indicates the presence of respective elements.

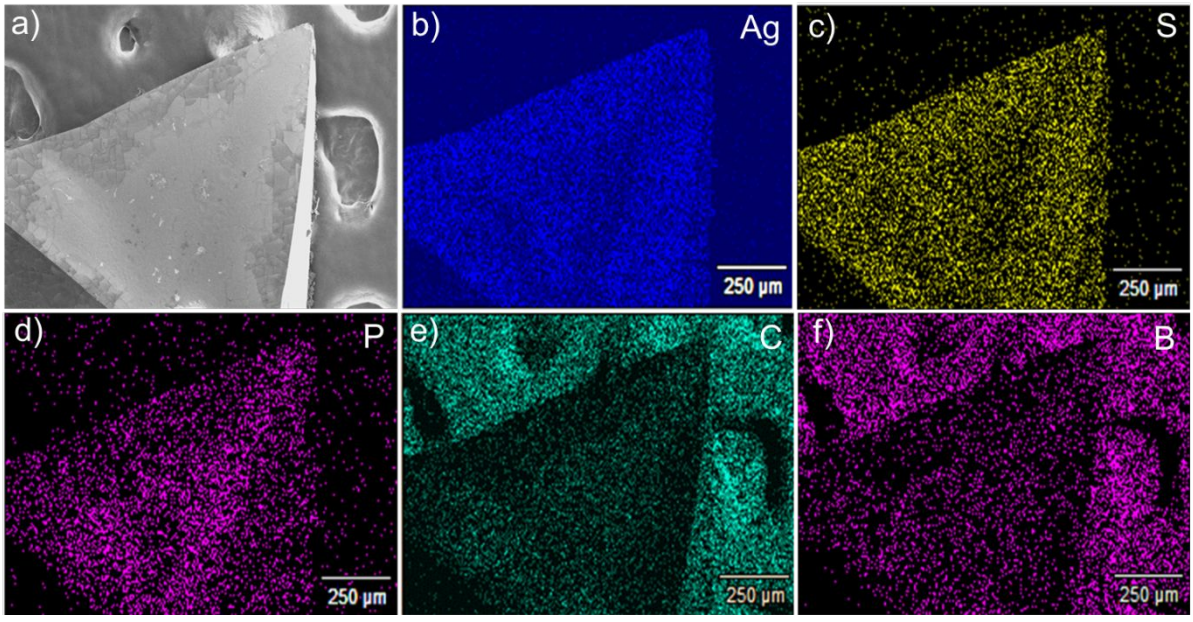

Figure S6. a) The FESEM image of a single crystal, b-f) the collected EDS elemental mapping of the same crystal, showing the respective elements of Ag, S, P, C and B, respectively.

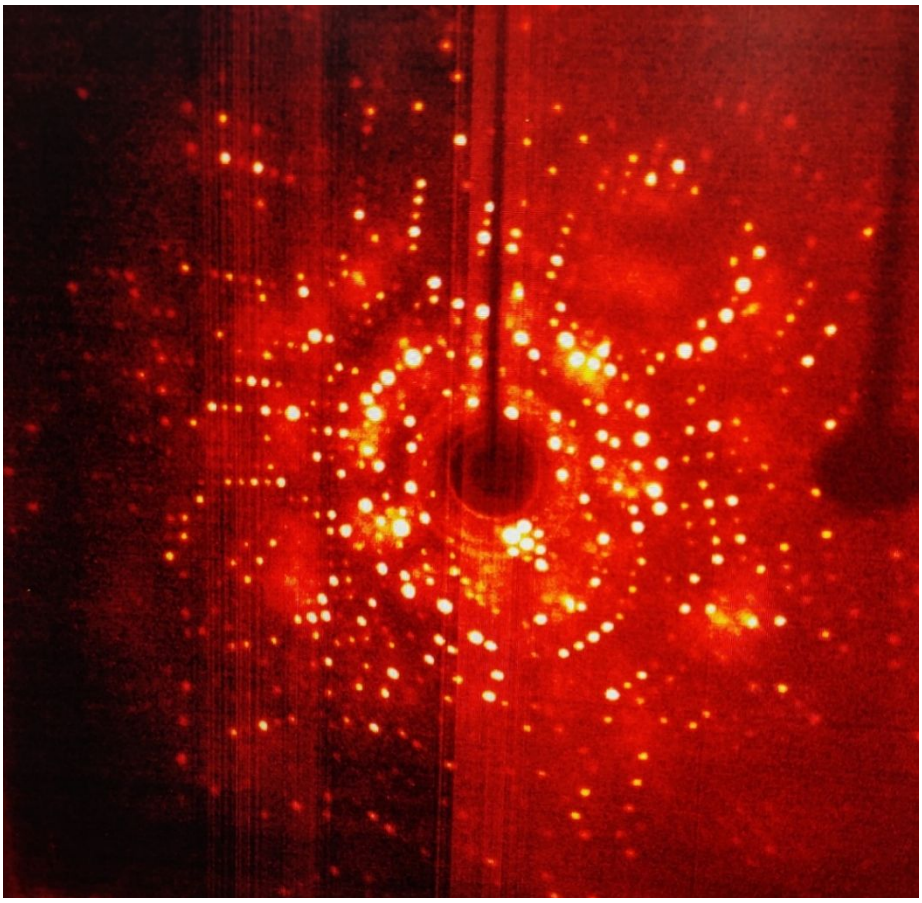

Figure S7. The collected frame of X-ray diffraction spots, indicating good crystallinity of these pyramidal crystals.

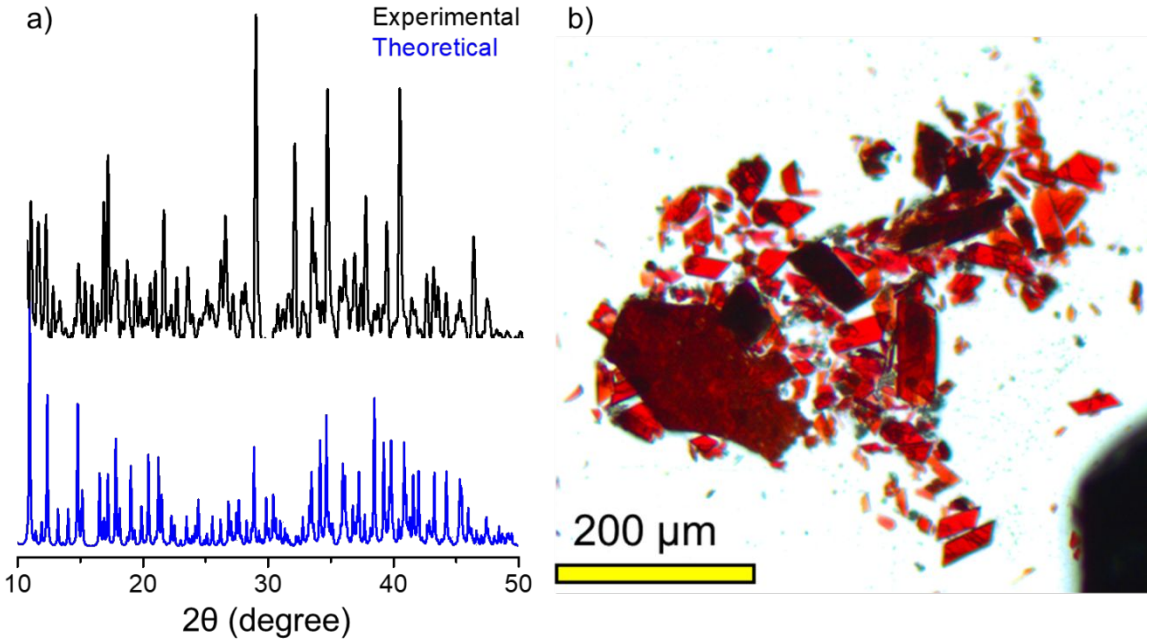

Figure S8. a) Experimental PXRD pattern of Ag_{21} microcrystals in comparison with the theoretical pattern. b) Microscopic image of respective microcrystals used for PXRD measurement.

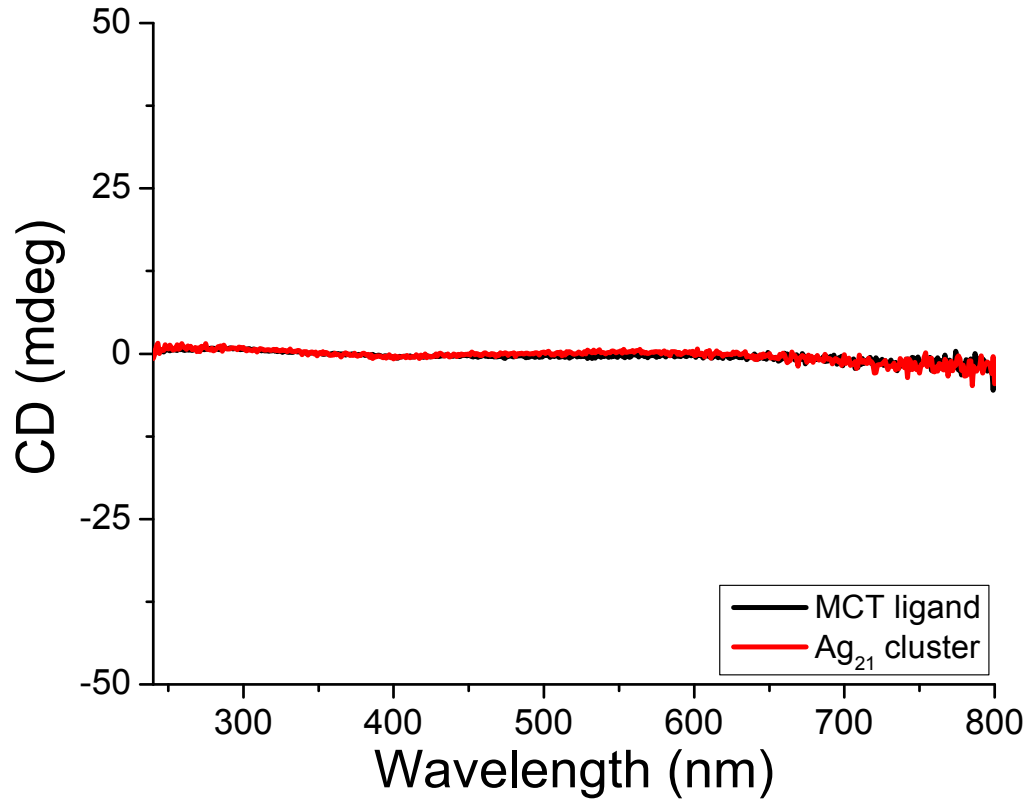

Figure S9. Circular dichroism (CD) spectra of Ag_{21} cluster along with MCT ligand. Nearly zero CD spectral signature indicates the achiral nature of the cluster in DCM solution.

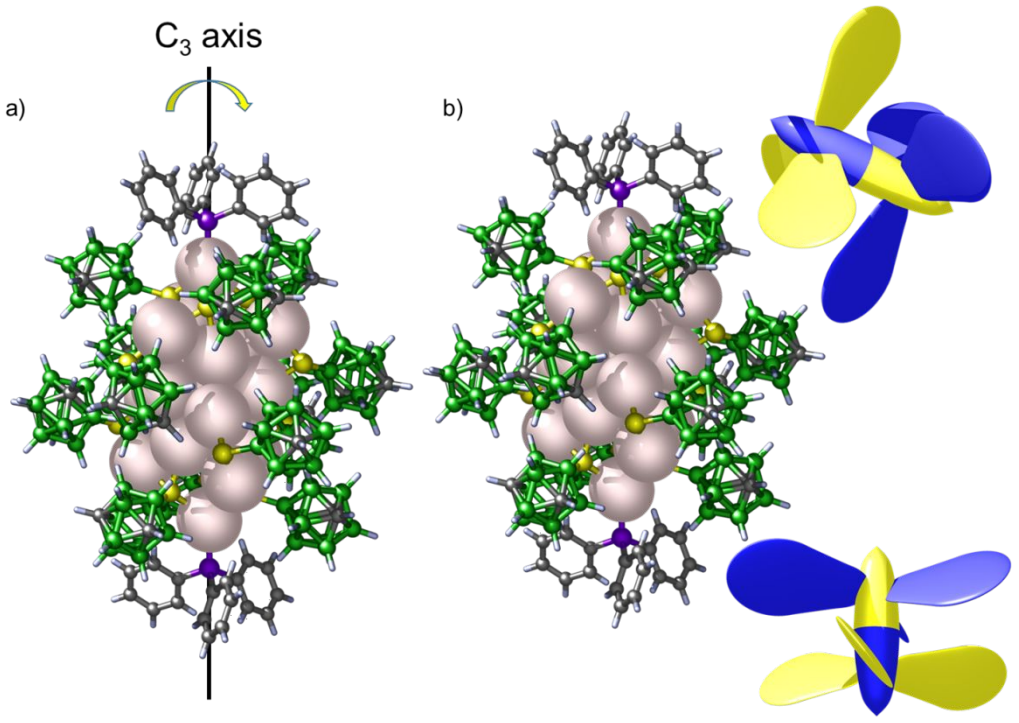

Figure S10. a) The C_3 axis present in the nanomolecule. b) Orientation of carboranes also viewed as an assembly of double rotors. Color code : light purple = silver, green = boron, violet = phosphorous, yellow = sulphur, black = carbon, white = hydrogen.

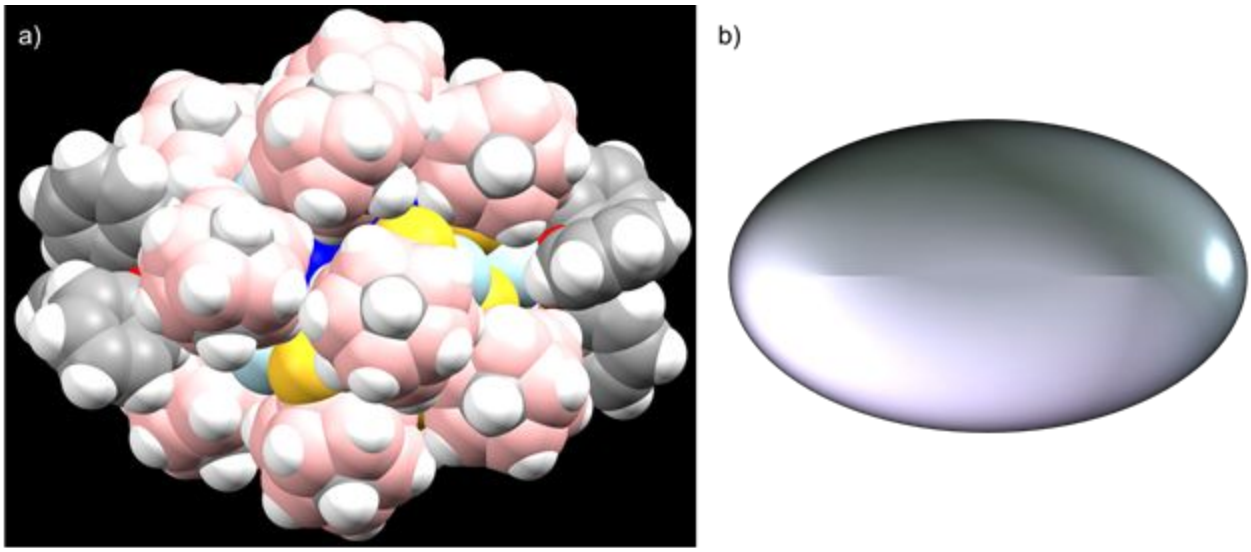

Figure S11. a) The space filling view of the Ag_{21} nanomolecule has two TPP in its head and tail positions. b) A schematic representation of oval shape, which correlates with the structure.

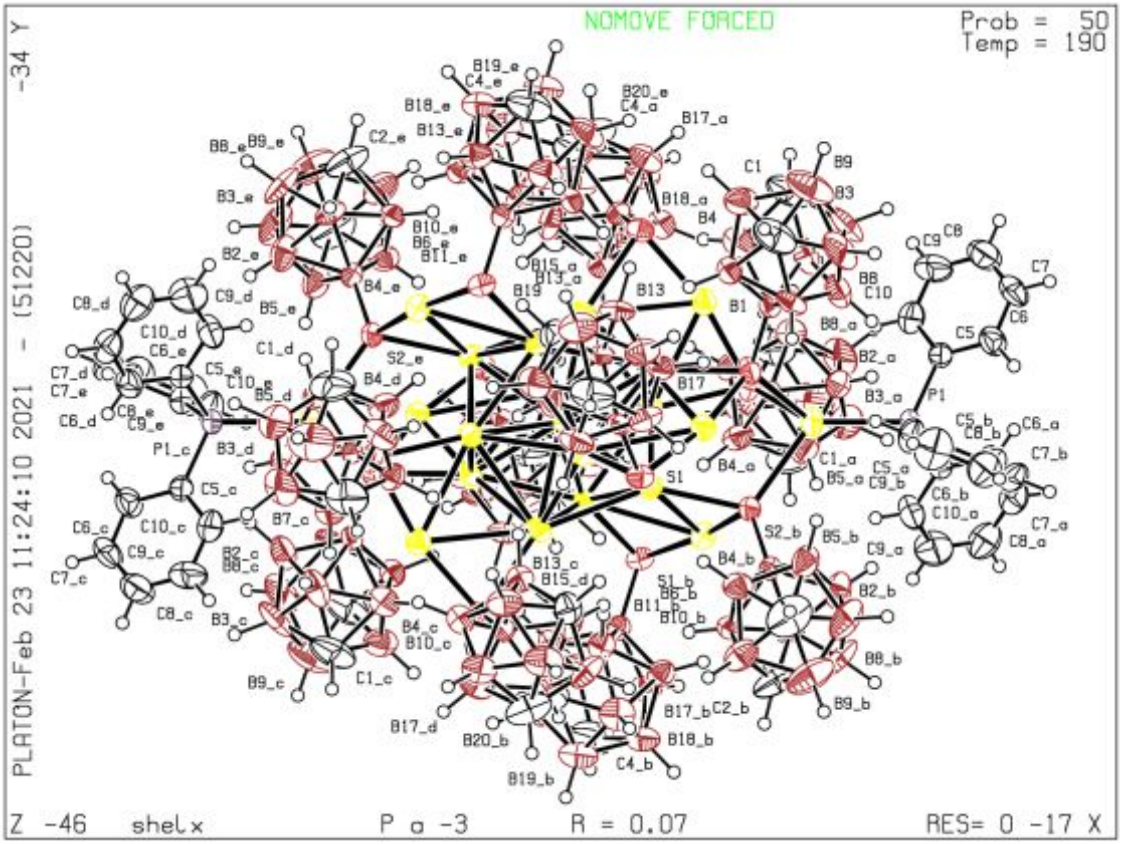

Figure S12. The ORTEP molecular structure of $[Ag_{21}(MCT)_{12}(TPP)_2]$ nanocluster.

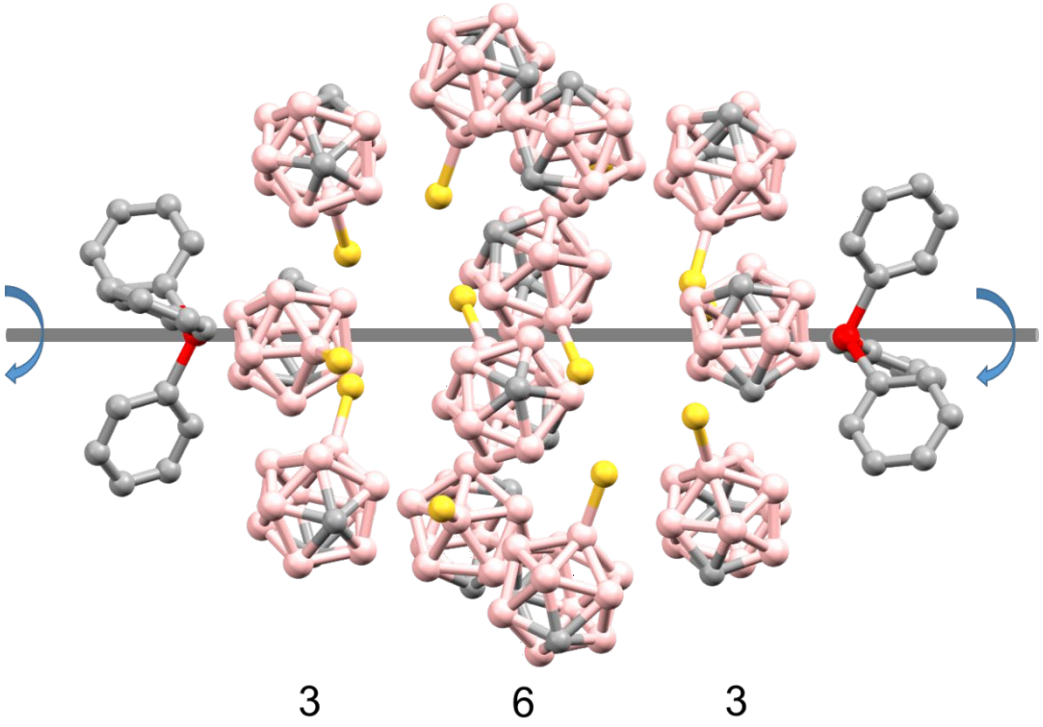

Figure S13. The arrangement of the twelve carborane ligands in 3: 6: 3 fashion along the P-P axis.

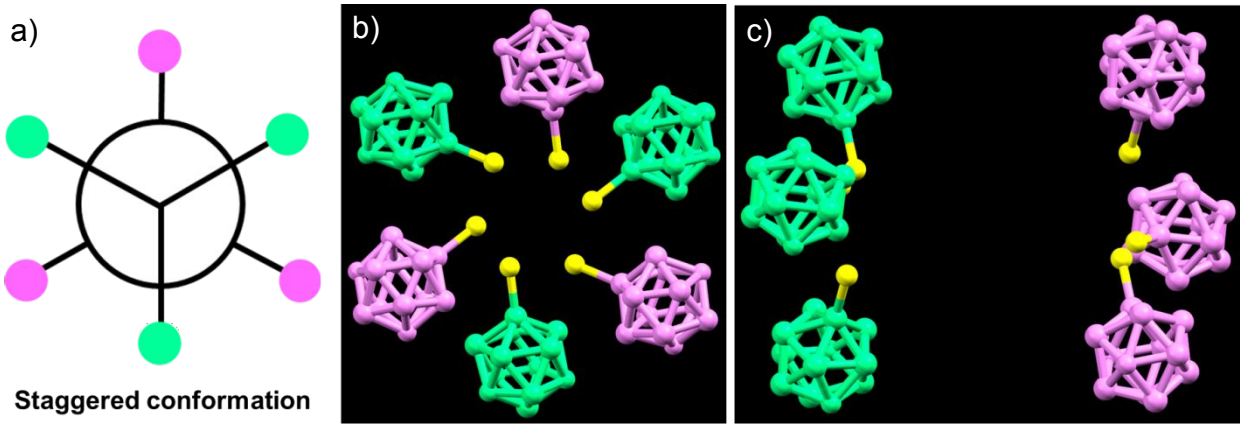

Figure S14. a) Schematic representation of the staggered conformation. b) Top view and c) side view of the respective carboranes. Atomic color code: green = top three carboranes and pink = bottom three carboranes.

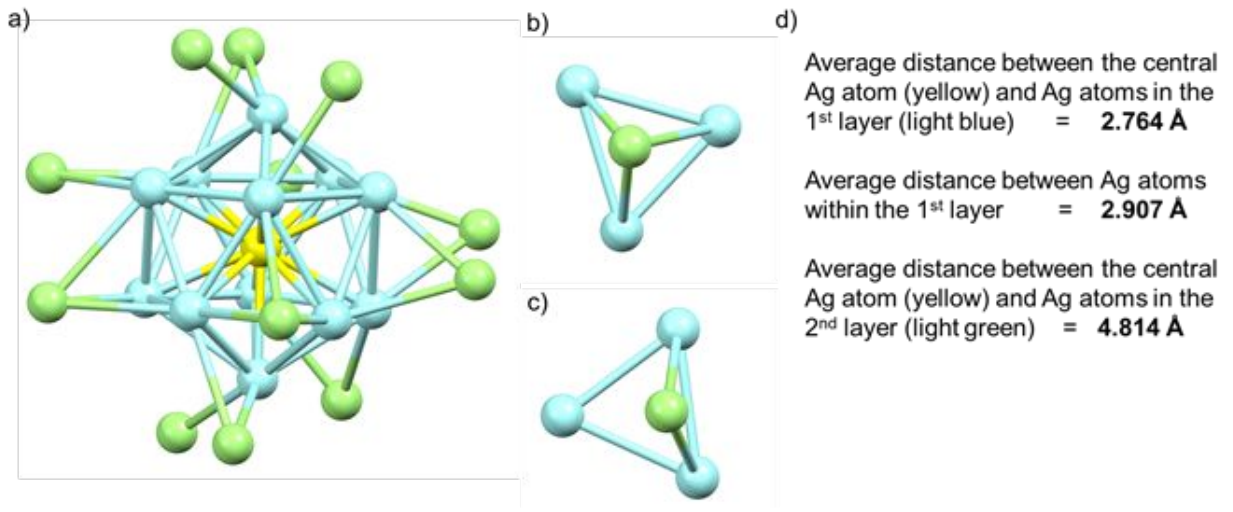

Figure S15. a) Atomic arrangements of the silver skeleton of Ag_{25} nanocluster. b) Close to face-centred (μ_3) outer shell Ag atom configuration. c) Bridging off-centred (μ_2) outer shell Ag atom configuration. d) Different types of average intermetallic Ag-Ag bond distances. All atoms presented are silver here.

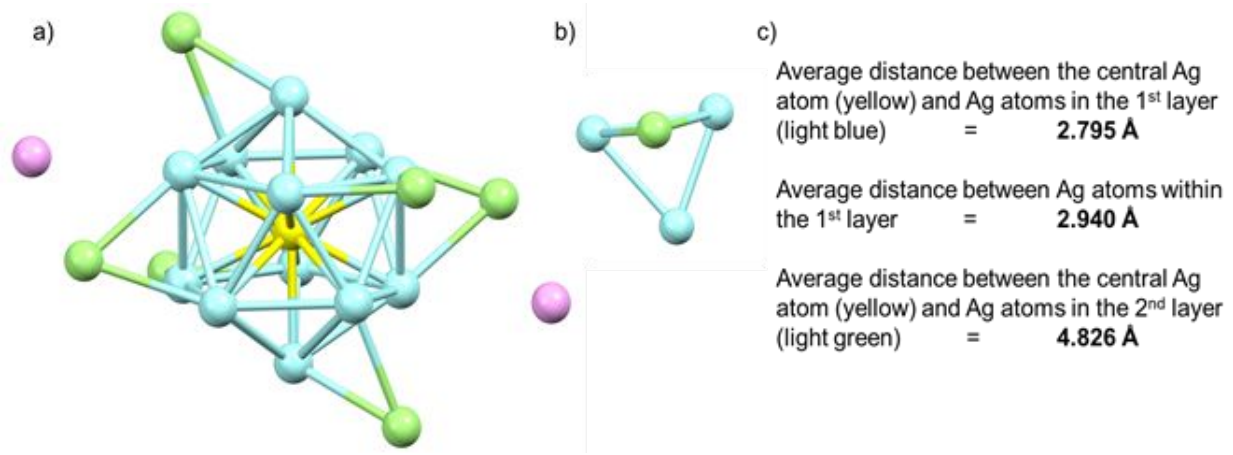

Figure S16. a) Atomic arrangements of the silver skeleton structure of our Ag_{21} nanocluster. b) Bridging off-centred (μ_2) outer shell Ag atom configuration. c) Different types of average intermetallic Ag-Ag bond distances. All atoms presented are silver here.

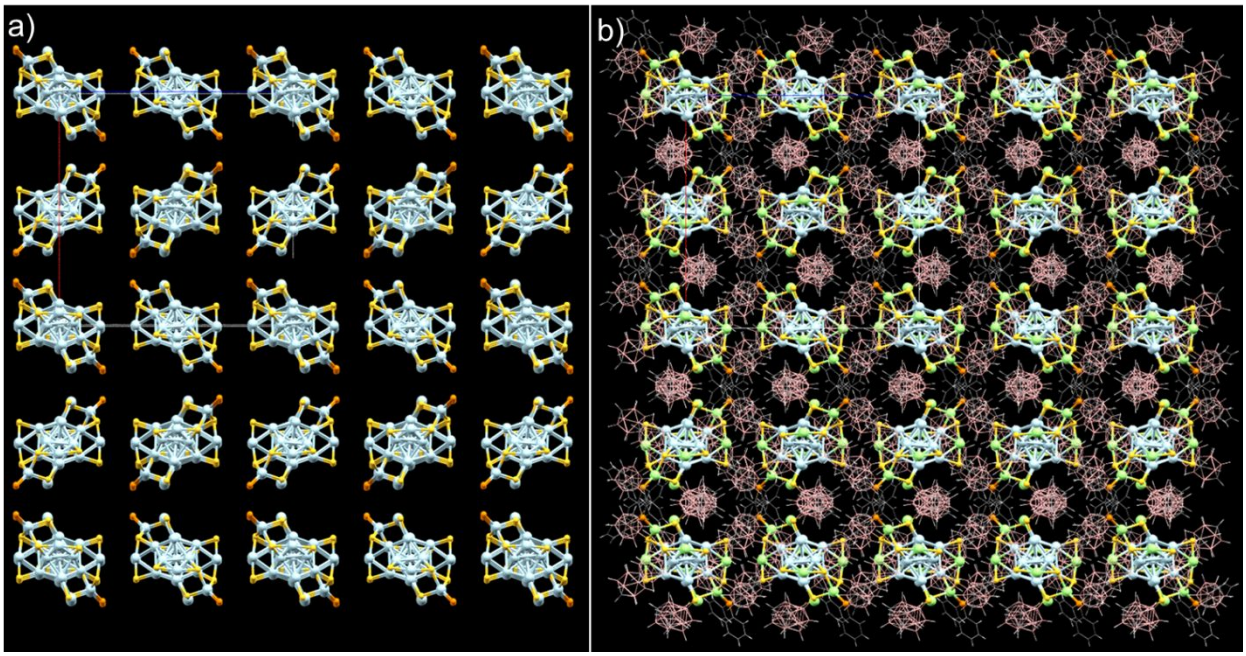

Figure S17. Extended view of intercluster packing along the axial direction of a) $Ag_{21}S_{12}P_2$ unit, and b) the full structure of Ag_{21} nanocluster with both MCT and TPP ligands.

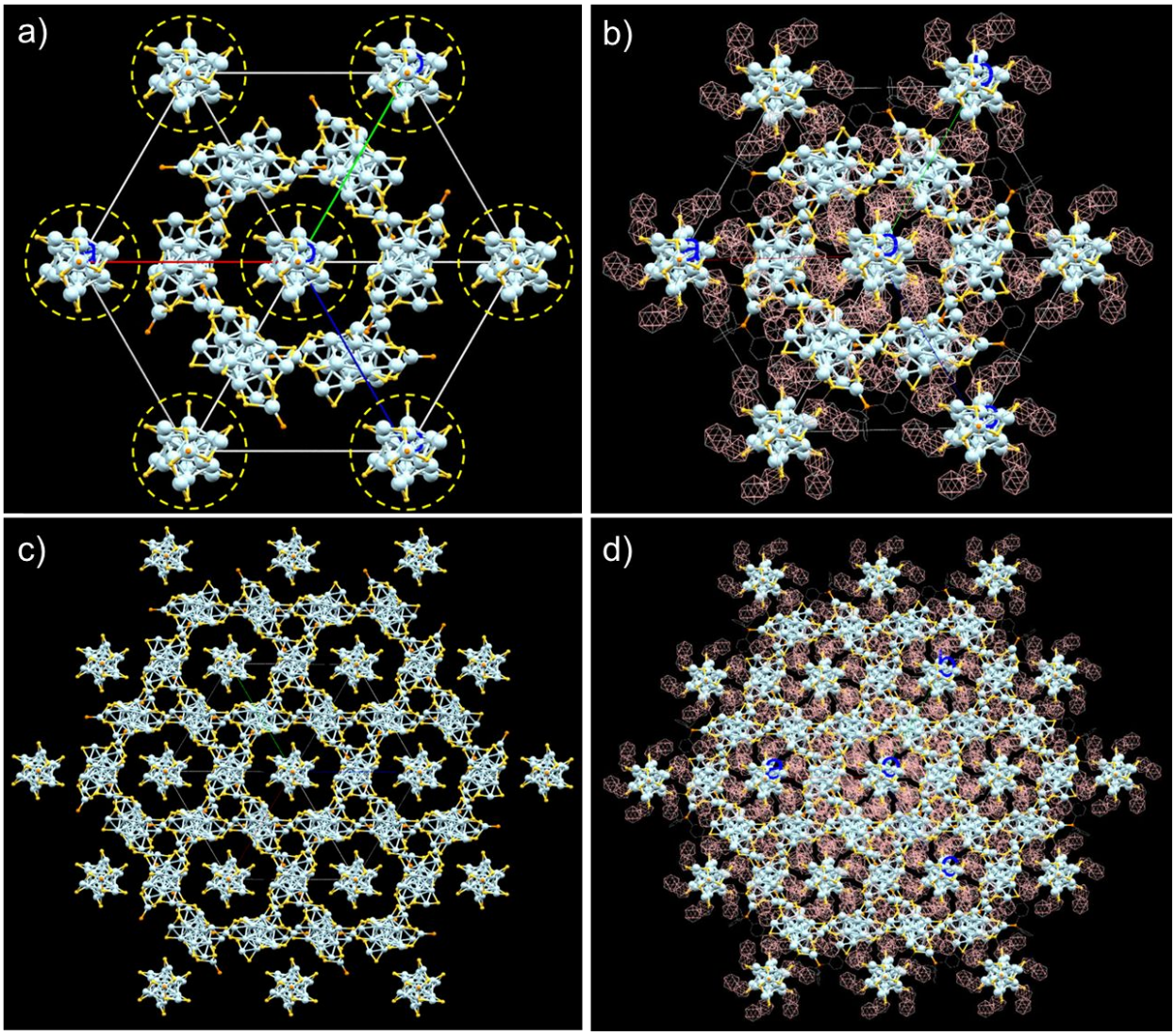

Figure S18. Intercluster packing along o-corner of the unit cell of a) $Ag_{21}S_{12}P_2$ unit and b) full structure of Ag_{21} nanocluster. Encircled clusters have propeller orientation. 2×2×2 packing of c) $Ag_{21}S_{12}P_2$ unit and d) full structure of Ag_{21} nanocluster. Hydrogen atoms are removed for clarity.

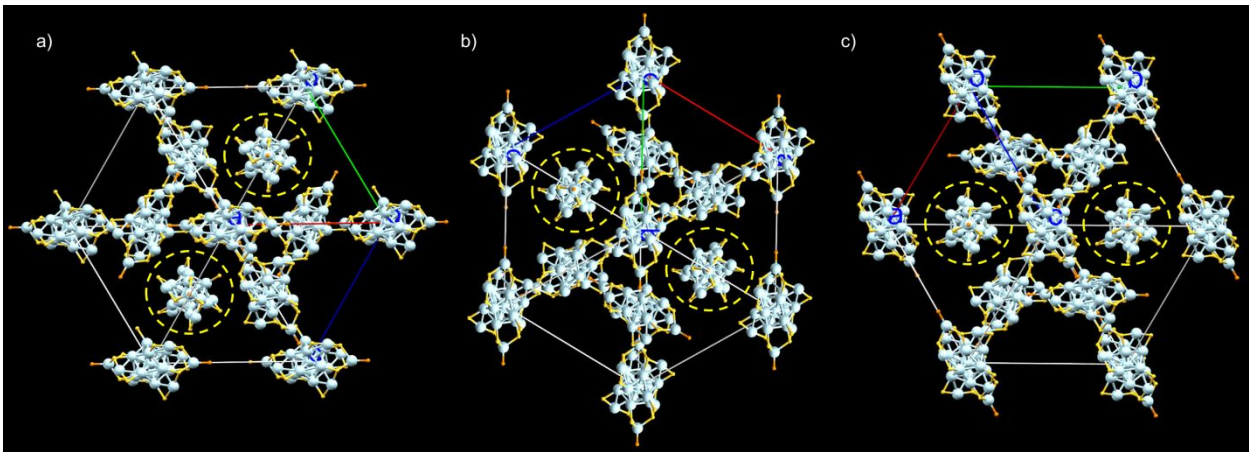

Figure S19. Intercluster packing of $Ag_{21}S_{12}P_2$ unit along a) a, b) b and c) c-corners of the unit cell of Ag_{21} nanocluster. Encircled clusters have propeller orientation.

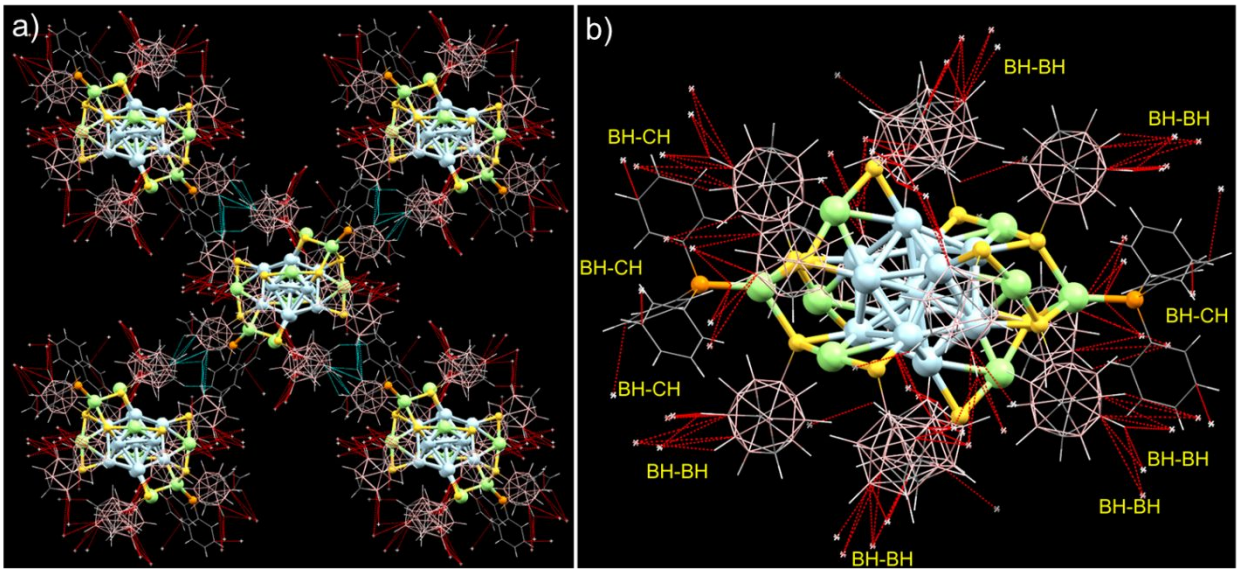

Figure S20. a, b) Intercluster packing of Ag_{21} shows the presence of several BH-BH and BH-CH interactions.

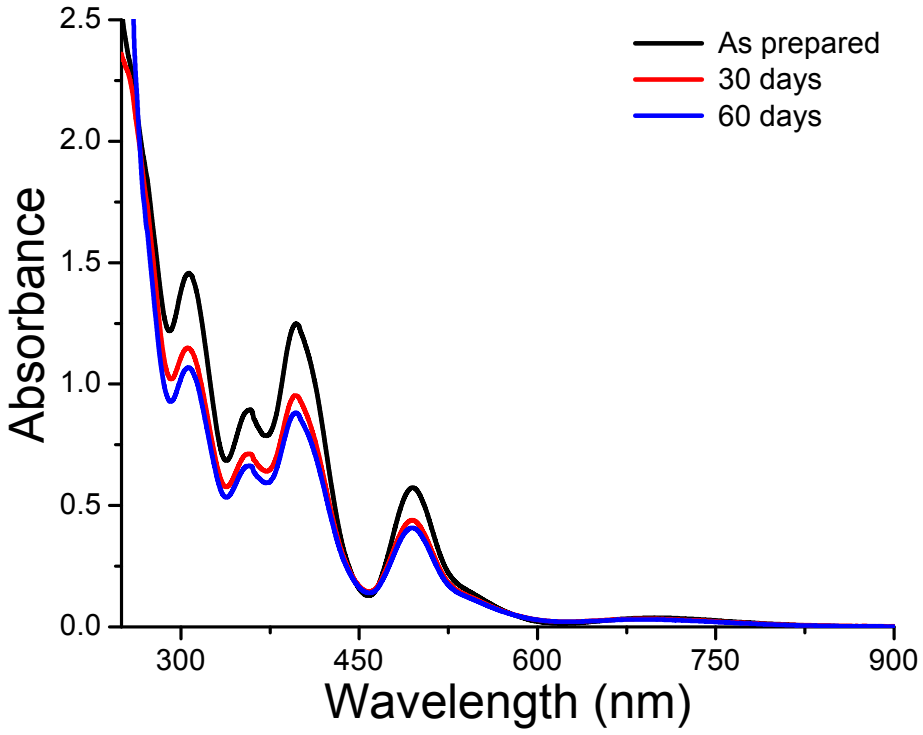

Figure S21. UV-vis absorption spectra of Ag_{21} nanocluster, indicating its stability up to 60 days.

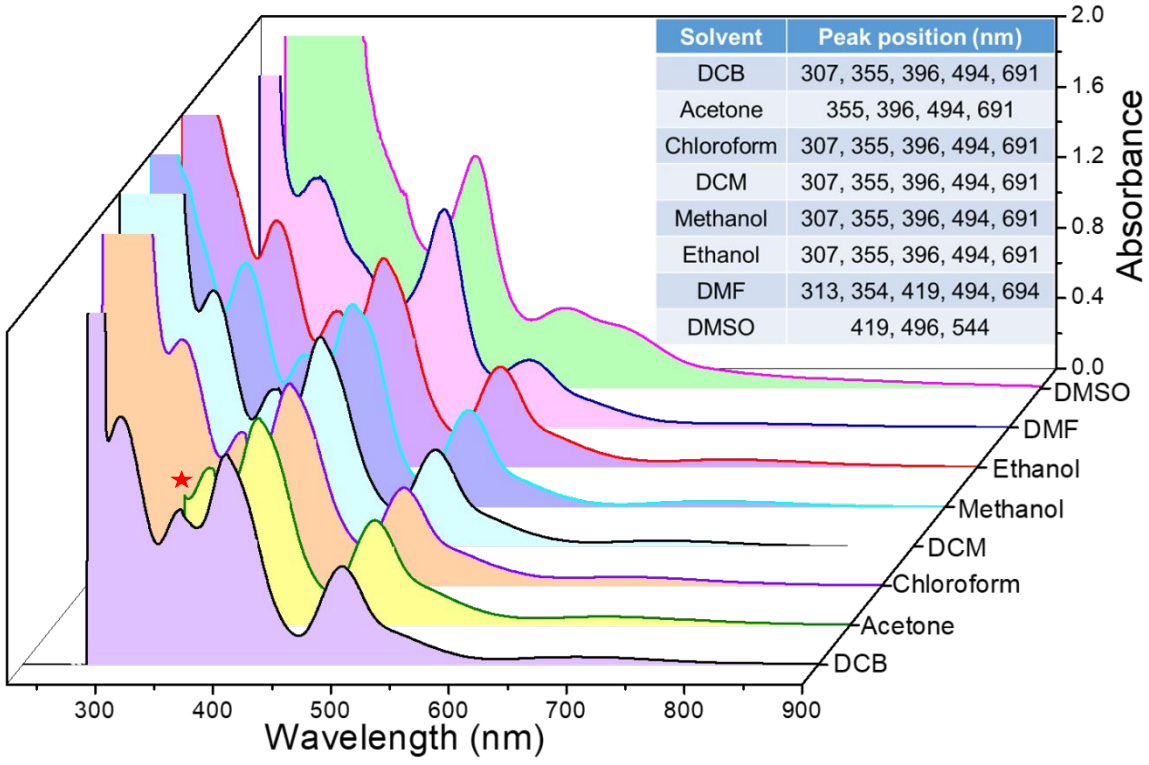

Figure S22. UV-vis absorption spectra of Ag_{21} nanocluster measured in different solvents. Identical peak pattern and position were observed in DCB, acetone, chloroform, DCM, methanol and ethanol solvents, whereas DMF and DMSO show difference in spectra due to solvatochromic effect. The inflection labeled * indicates spectral cut-off in acetone.

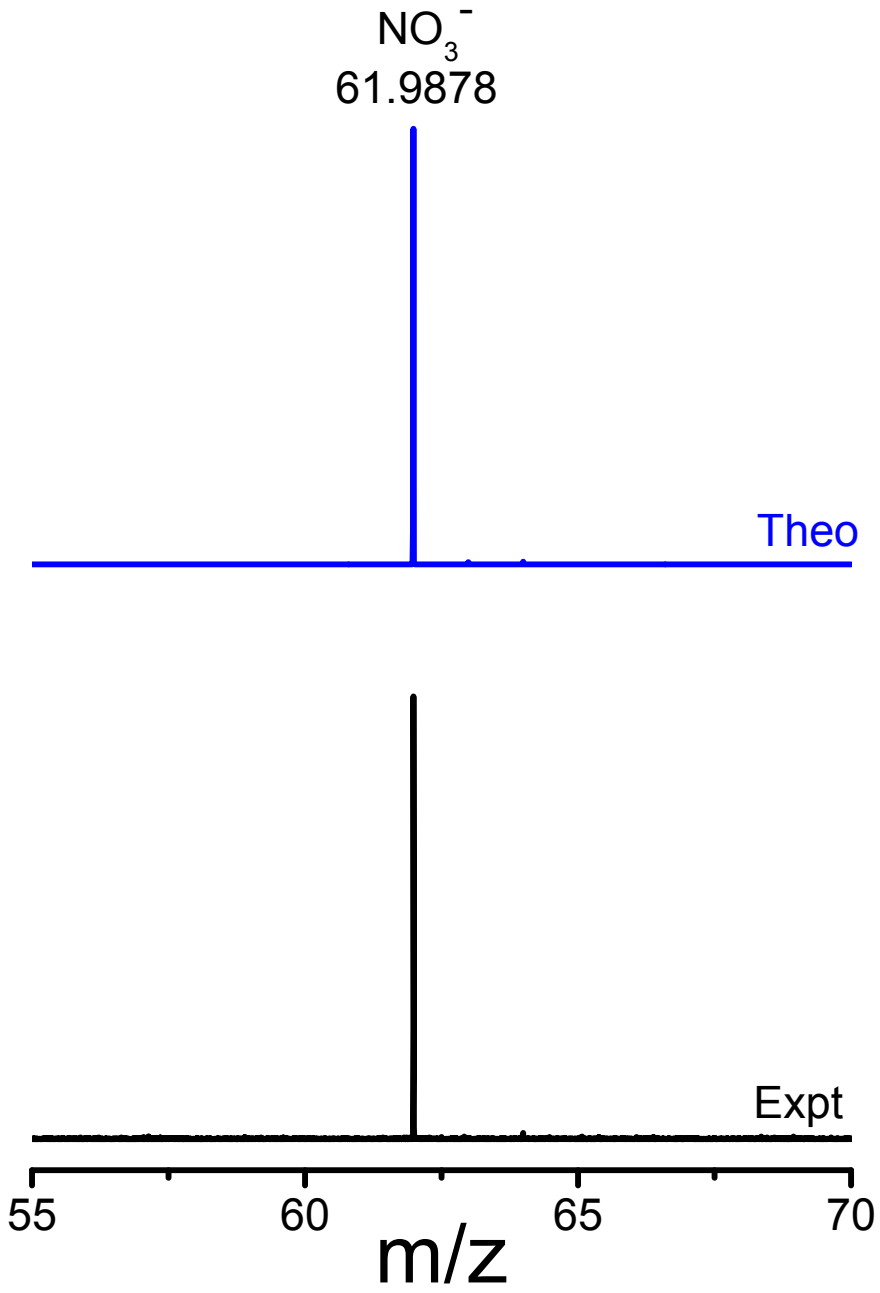

Figure S23. The experimental mass spectrum of Ag_{21} crystals in negative ion mode shows the presence of NO_3^- as a counter ion in the crystals.

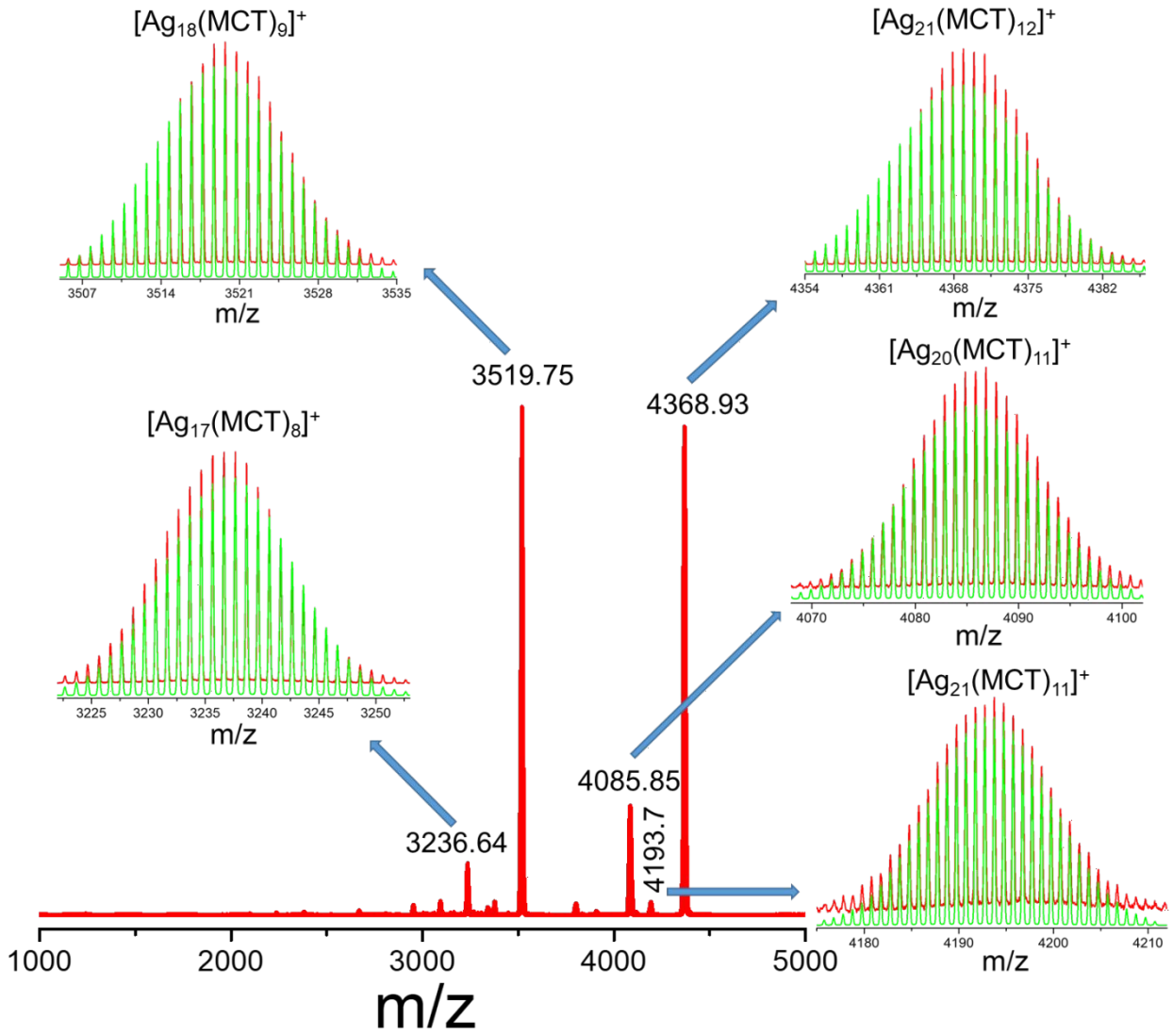

Figure S24. Expanded view of the MS/MS fragmentation spectrum at CE 75 in positive ion mode, indicating systematic loss of MCT and Ag units. Color codes: red = experimental spectrum; green = theoretical spectrum.

Table S3. Correlations between peak intensity and valence electron count of fragmented peaks formed at higher collision energy.

Sl No	Clusters	Electron counting [Ne-L-q]	Remarks	Peak intensity
1	$[Ag_{21}(MCT)_{12}(TPP)_2]^+$	[21-12-1] = 8	Magic electrons	High
2	$[Ag_{21}(MCT)_{12}(TPP)]^+$	[21-12-1] = 8	Magic electrons	High
3	$[Ag_{21}(MCT)_{12}]^+$	[21-12-1] = 8	Magic electrons	High
4	$[Ag_{21}(MCT)_{11}]^+$	[21-11-1] = 9	Non-magic electrons	Low
5	$[Ag_{20}(MCT)_{11}]^+$	[20-11-1] = 8	Magic electrons	High
6	$[Ag_{20}(MCT)_{10}]^+$	[20-10-1] = 9	Non-magic electrons	Low
7	$[Ag_{19}(MCT)_{10}]^+$	[19-10-1] = 8	Magic electrons	High
8	$[Ag_{19}(MCT)_9]^+$	[19-9-1] = 9	Non-magic electrons	Low
9	$[Ag_{18}(MCT)_9]^+$	[18-9-1] = 8	Magic electrons	High
10	$[Ag_{18}(MCT)_8]^+$	[18-8-1] = 9	Non-magic electrons	Low
11	$[Ag_{17}(MCT)_8]^+$	[17-8-1] = 8	Magic electrons	High
12	$[Ag_{17}(MCT)_7]^+$	[17-7-1] = 9	Non-magic electrons	Low
13	$[Ag_{16}(MCT)_7]^+$	[16-7-1] = 8	Magic electrons	High
14	$[Ag_{16}(MCT)_6]^+$	[16-6-1] = 9	Non-magic electrons	Low
15	$[Ag_{15}(MCT)_6]^+$	[15-6-1] = 8	Magic electrons	High

16	$[Ag_{15}(MCT)_5]^+$	[15-5-1] = 9	Non-magic electrons	Low
17	$[Ag_{14}(MCT)_5]^+$	[14-5-1] = 8	Magic electrons	High
18	$[Ag_{14}(MCT)_4]^+$	[14-4-1] = 9	Non-magic electrons	Low
19	$[Ag_{13}(MCT)_4]^+$	[13-4-1] 8	Magic electrons	High

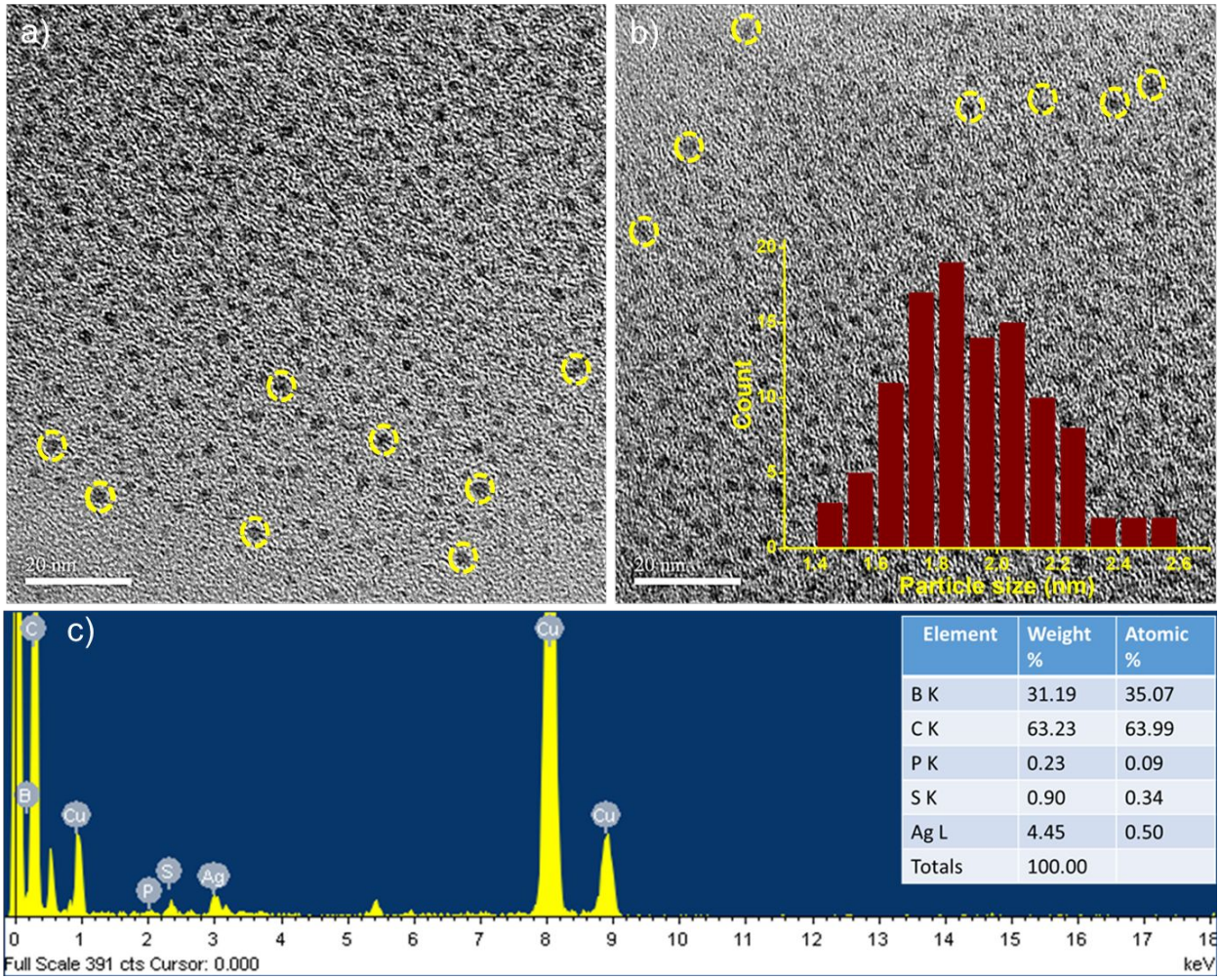

Figure S25. a, b) TEM images of the Ag_{21} nanocluster showed its particle nature. Inset shows the size distribution profile of 100 particles. Average particle dimension is 1.91±0.2 nm. c) The EDS spectrum of the nanocluster shows the existing elements (inset shows the atomic and elemental weight % of the existing elements).

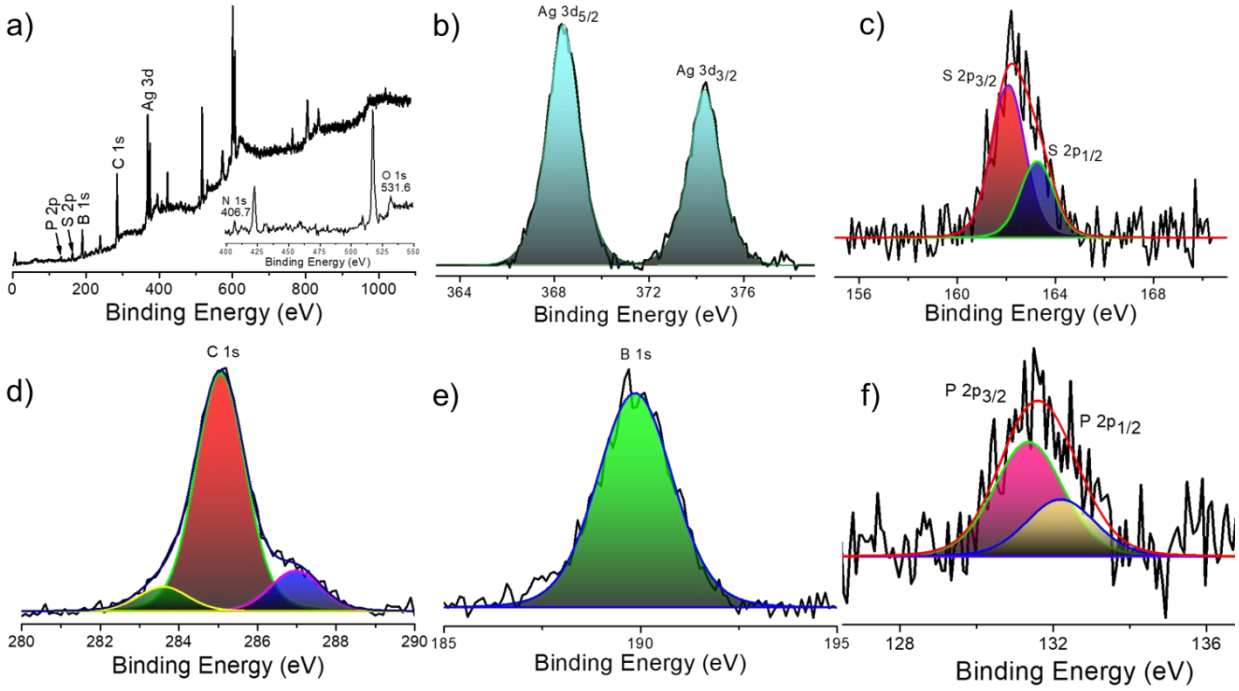

Figure S26. a) XPS survey spectrum of Ag_{21} nanocluster showed the spectral signature of respective elements. Inset shows the N 1s and O 1s peaks at 406.7 and 531.6 eV, respectively due to nitrate counter ion. Spectral fitting of b) Ag 3d region, c) S 2p region, d) C 1s region, e) B 1s region and f) P 2p region.

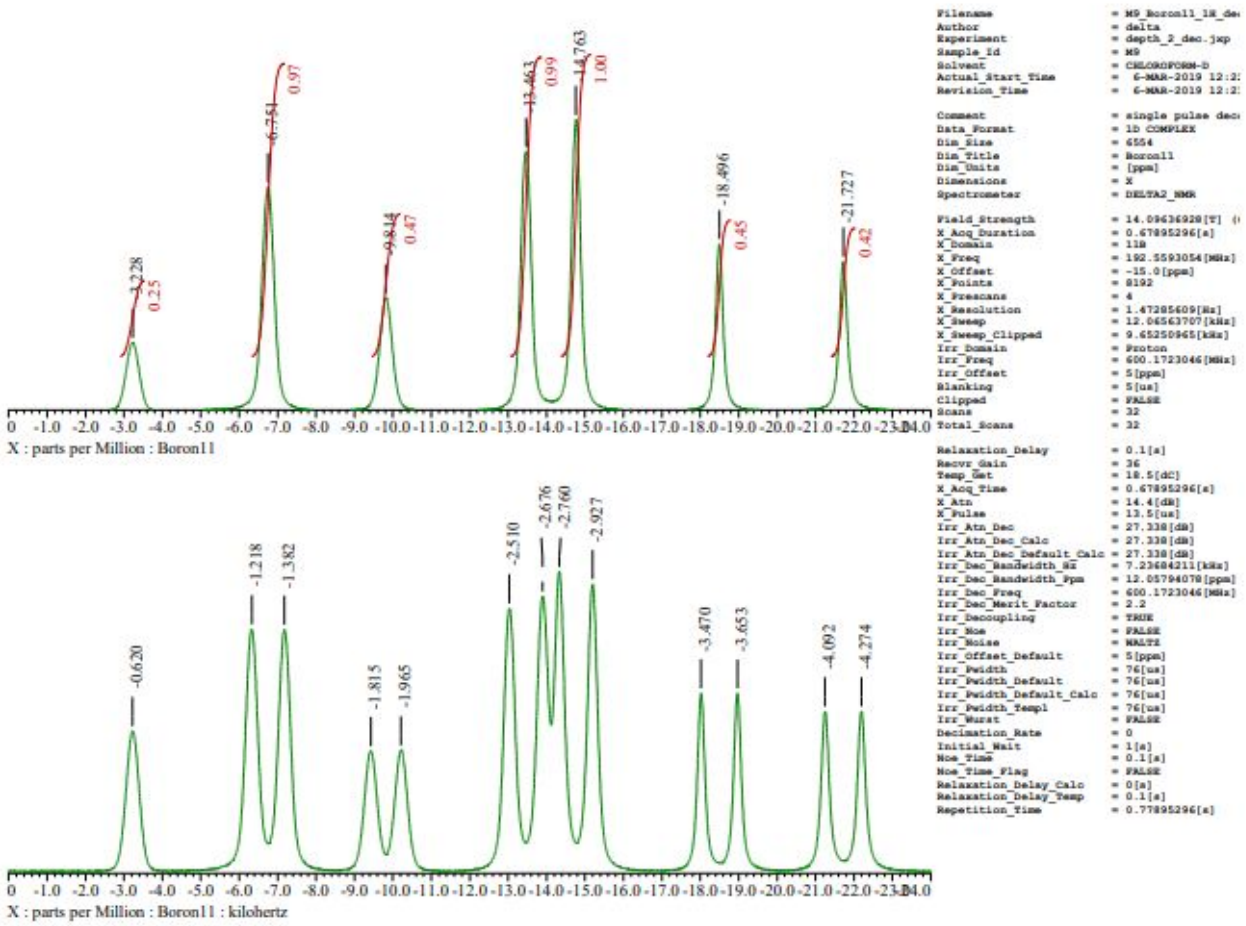

Figure S27. ^{11}B NMR spectrum of MCT ligand in $CDCl_3$ solvent.

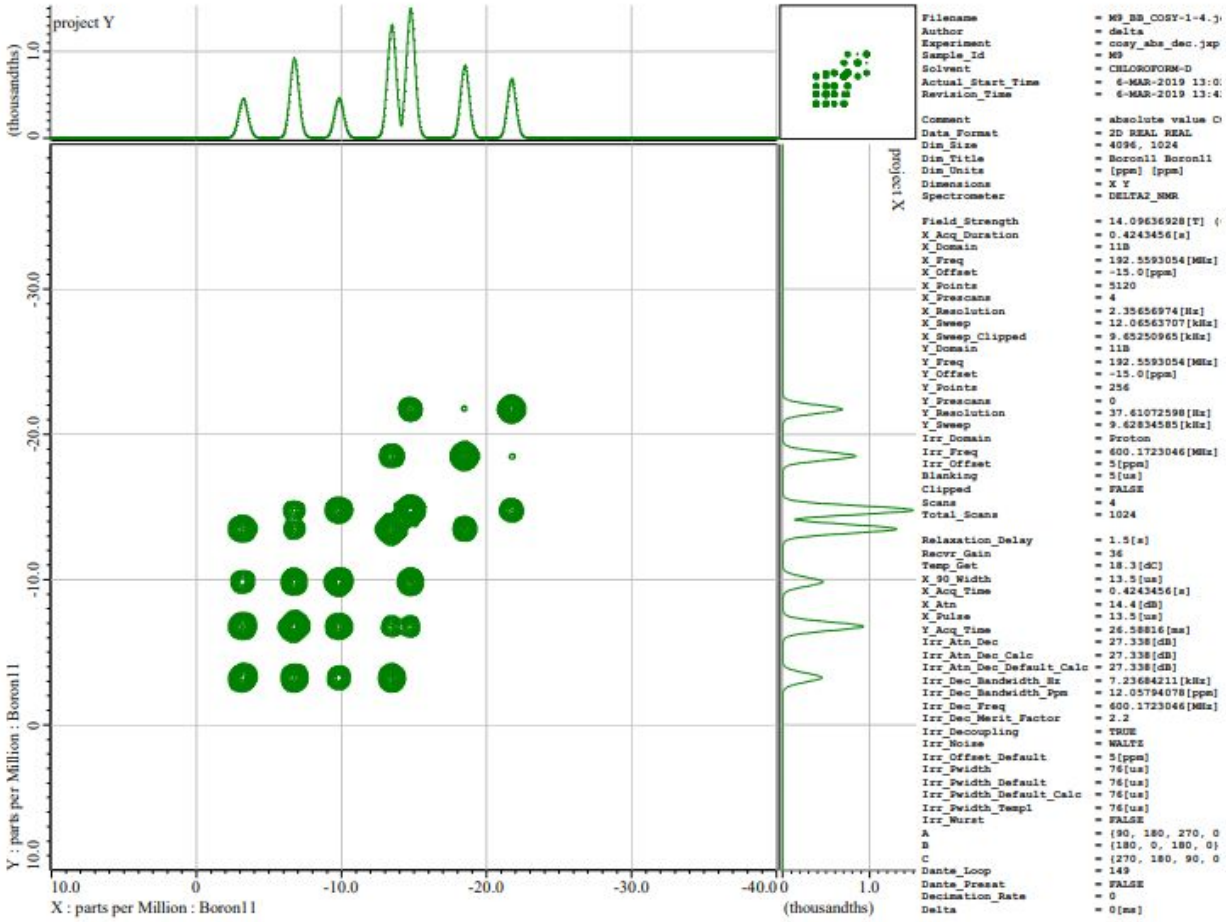

Figure S28. ^{11}B-^{11}B COSY NMR spectrum of MCT ligand in $CDCl_3$ solvent.

Table S4. ^{11}B NMR chemical shift data for the MCT ligand, measured in $CDCl_3$ solvent.

	MCT
Assign.	$\delta(^{11}B)$
1,7	-
2	–18.5
3,8	–14.8
4,12	–6.8
5,11	–13.5
6	–21.7
9	–3.2
10	–9.8

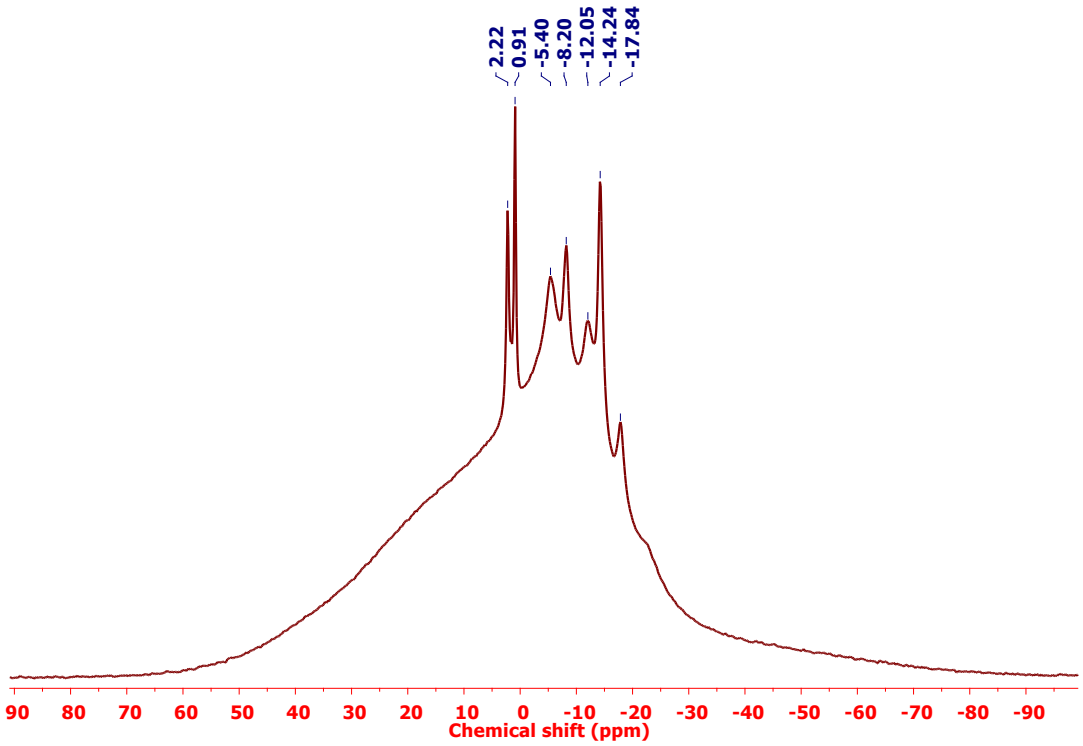

Figure S29. ^{11}B NMR spectrum of Ag_{21} nanocluster in $CDCl_3$ solvent.

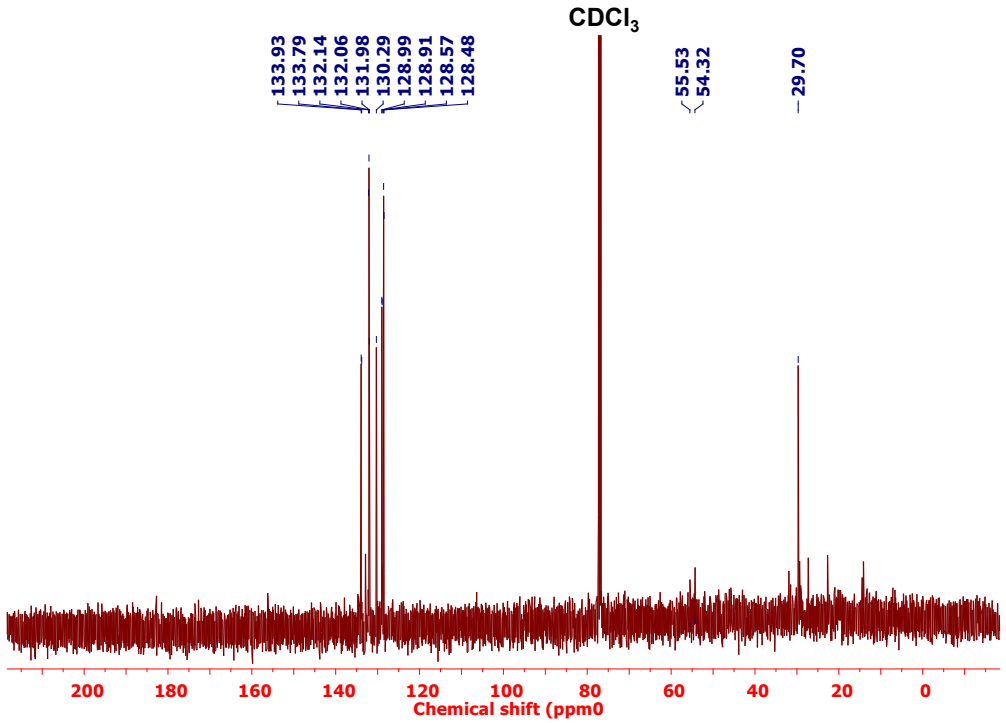

Figure S30. Proton-decoupled ^{13}C NMR spectrum of Ag_{21} nanocluster in $CDCl_3$ solvent.

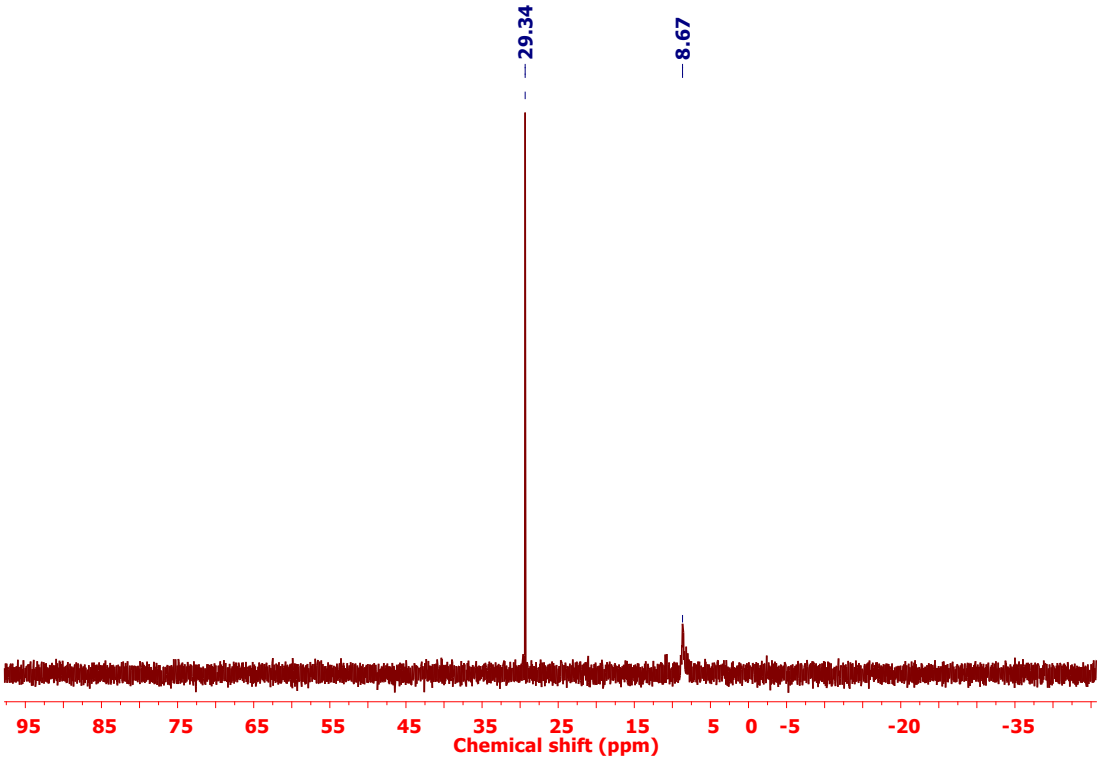

Figure S31. ^{31}P NMR spectrum of Ag_{21} nanocluster in $CDCl_3$ solvent.

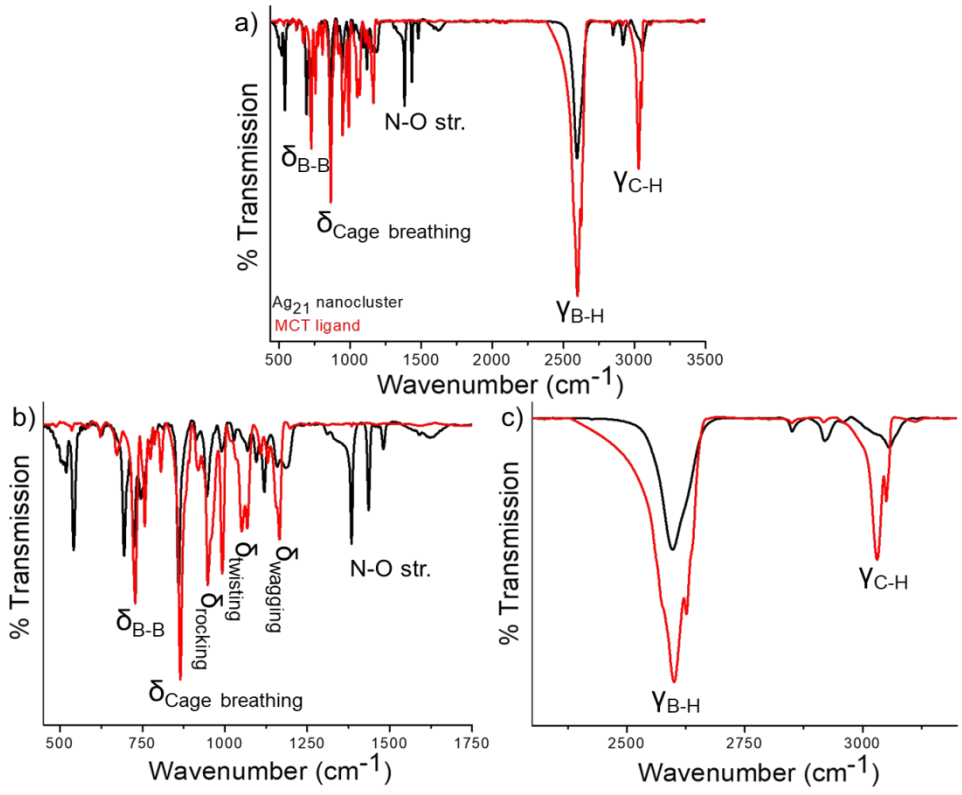

Figure S32. a) The full range FT-IR spectra of Ag_{21} in comparison with MCT ligands, b, c) expanded view of two different spectral regions, indicate the shifts of vibrational and rotational spectral features.

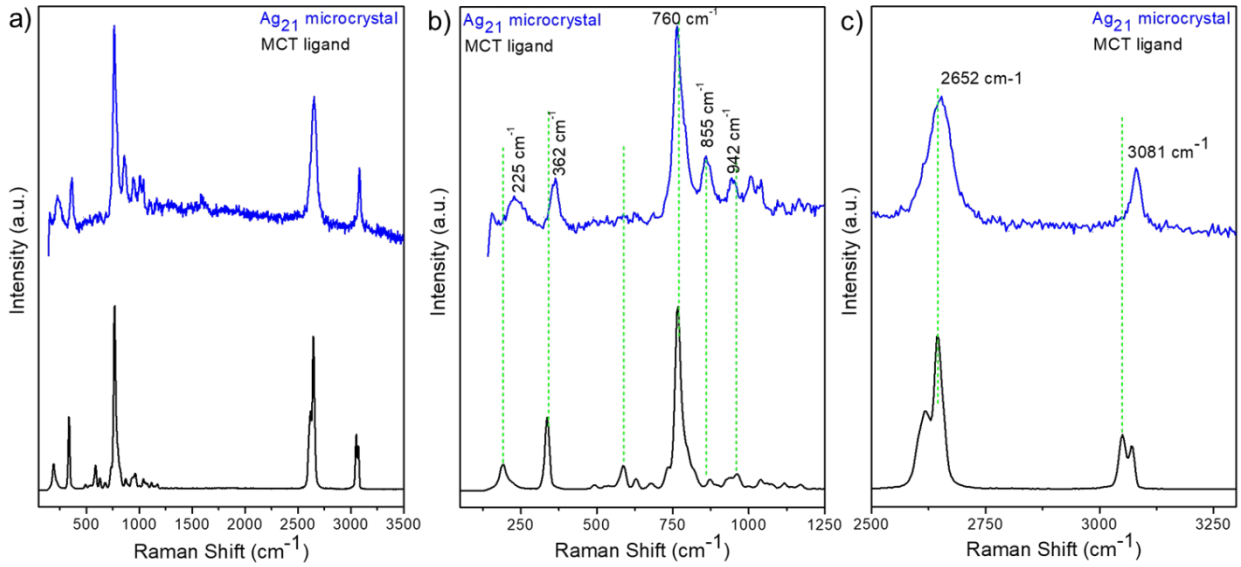

Figure S33. a) Full range comparative Raman spectra of Ag_{21} microcrystals along with MCT ligands, b, c) expanded view of two different spectral regions.

Table S5. Spectral assignments of vibrational Raman features of MCT ligand.

Sl No	Peak position (cm^{-1})	Spectral assignments
1.	3051, 3070	C-H stretching mode
2.	2618, 2645	B-H stretching mode + small contribution of S-H stretching mode
3.	1117, 1170	C-H bending mode
4.	1038, 1074	B-H bending mode
5.	871, 960	BBH bending mode
6.	762	Icosahedral breathing mode / pulsation of icosahedral cage
7.	586, 630, 678	BBB and BBC breathing mode
8.	191, 335, 491	B-B, B-S and B-C vibrational mode (decides cage regidity)

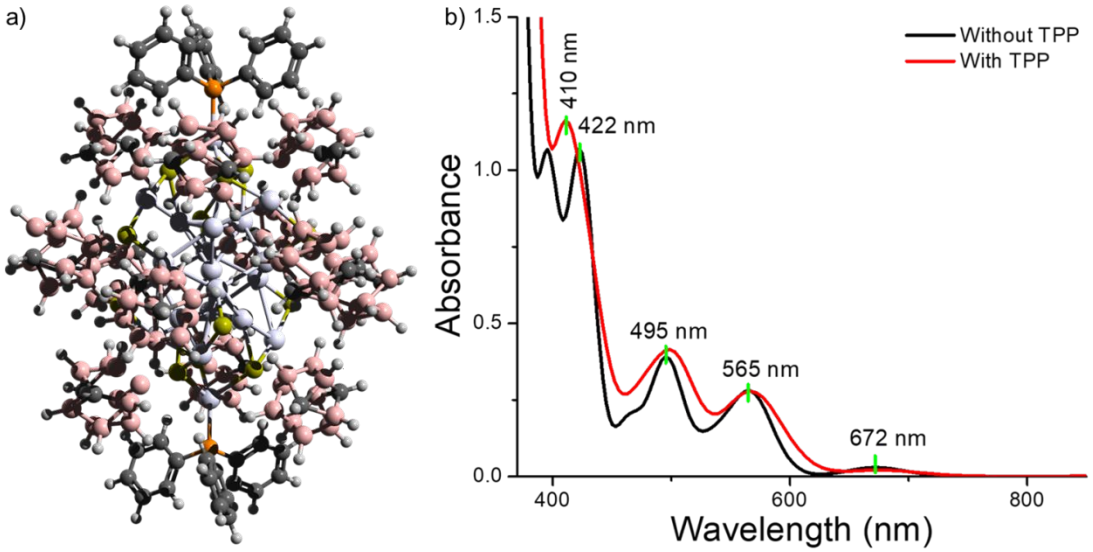

Figure 34. a) Theoretically optimized structure of Ag_{21} nanomolecule along with two TPP ligands. Color code: grey = silver, yellow = sulphur, pink = boron, black = carbon, orange = phosphorous, white = hydrogen. b) Theoretical absorption spectra showing nearly similar spectral feature for both the structures.

Table S6. Calculated oscillator strengths (f) of transitions.

Sl. no	Respective transition (nm)	f (Without TPP)	f (With TPP)
1.	672	0.0291	0.0210
2.	565	0.280	0.270
3.	494	0.391	0.0414
4.	422	1.070	-
5.	410	-	1.0067

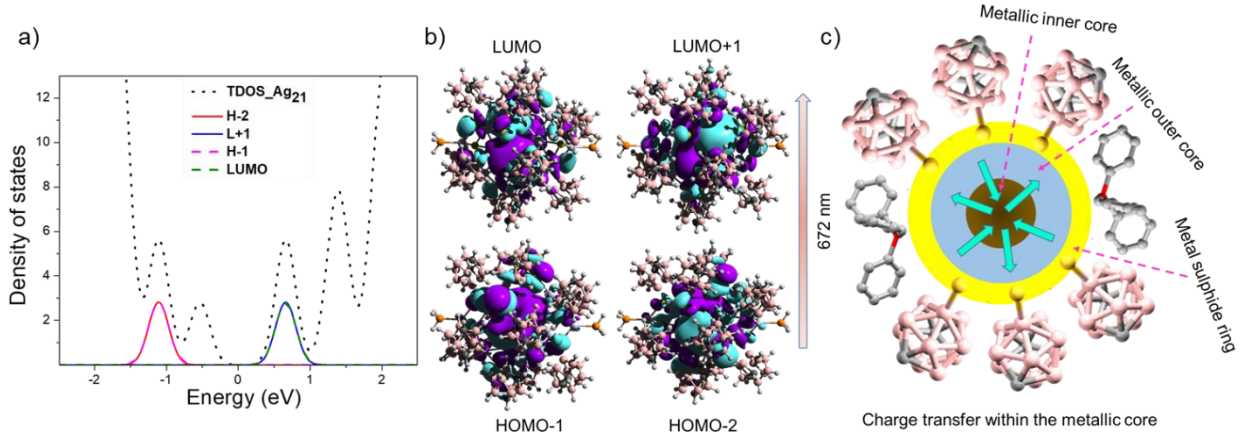

Figure S35. a) The DOS plots of molecular orbitals with the energy contribution for the transition at 672 nm. b) The electron density maps of molecular orbitals associated with the transition. c) Schematic representation shows associated charge transfer within the metallic core.

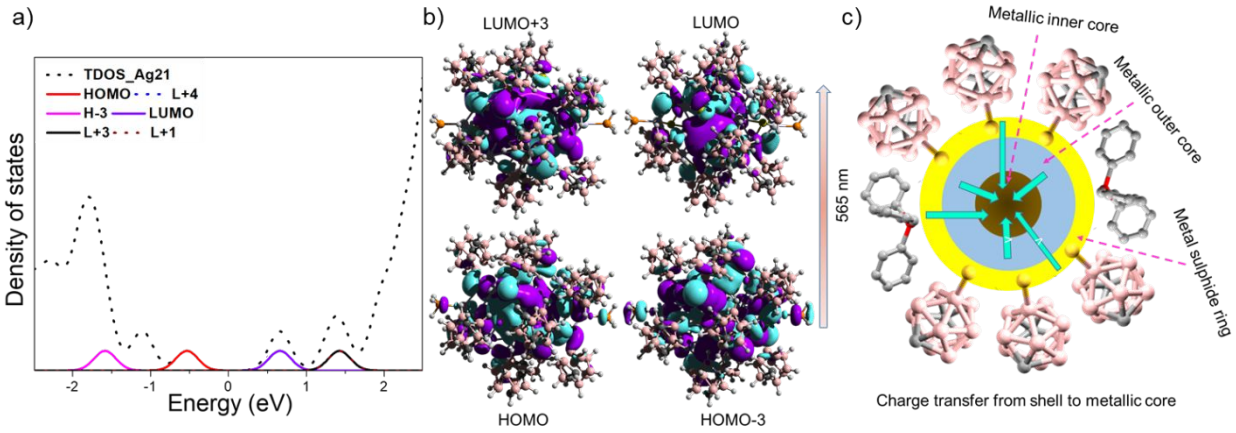

Figure S36. a) The DOS plots of molecular orbitals with the energy contribution for the transition at 565 nm. b) The electron density maps of molecular orbitals associated with the transition. c) Schematic representation shows associated charge transfer from the shell to the metallic core.

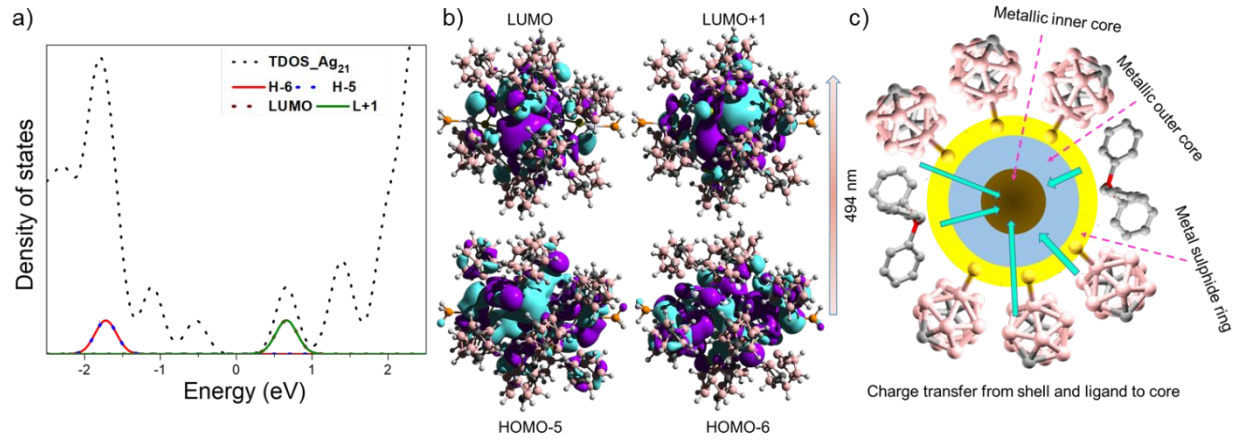

Figure S37. a) The DOS plots of molecular orbitals with the energy contribution for the transition at 494 nm. b) The electron density maps of molecular orbitals associated with the transition. c) Schematic representation shows associated charge transfer from the shell and ligand to the metallic core.

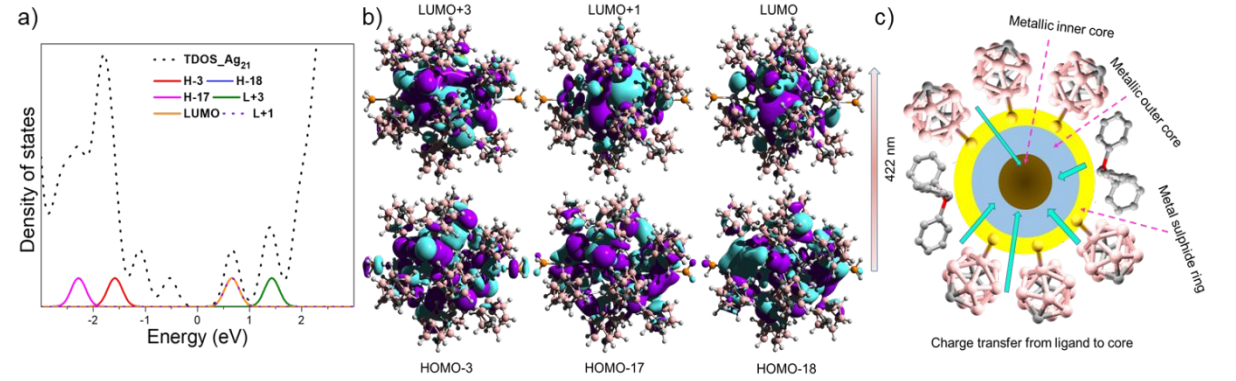

Figure S38. a) The DOS plots of molecular orbitals with the energy contribution for the transition at 422 nm. b) The electron density maps of molecular orbitals associated with the transition. c) Schematic representation shows associated charge transfer from the ligand to the metallic core.

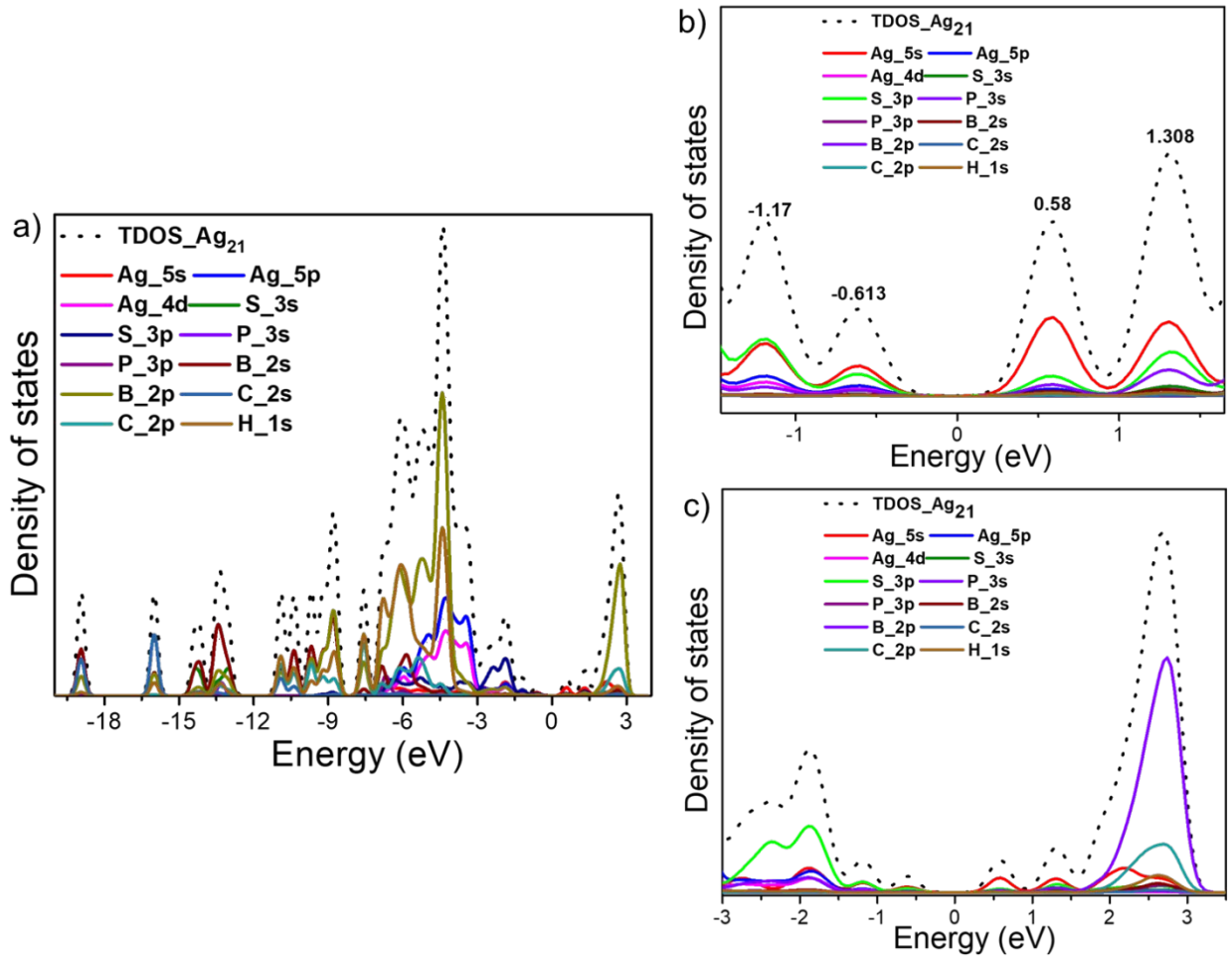

Figure S39. a) The full range density of states (DOS) in terms of atomic orbitals contribution. b, c) Enlarged view of the same spectrum for clarity.

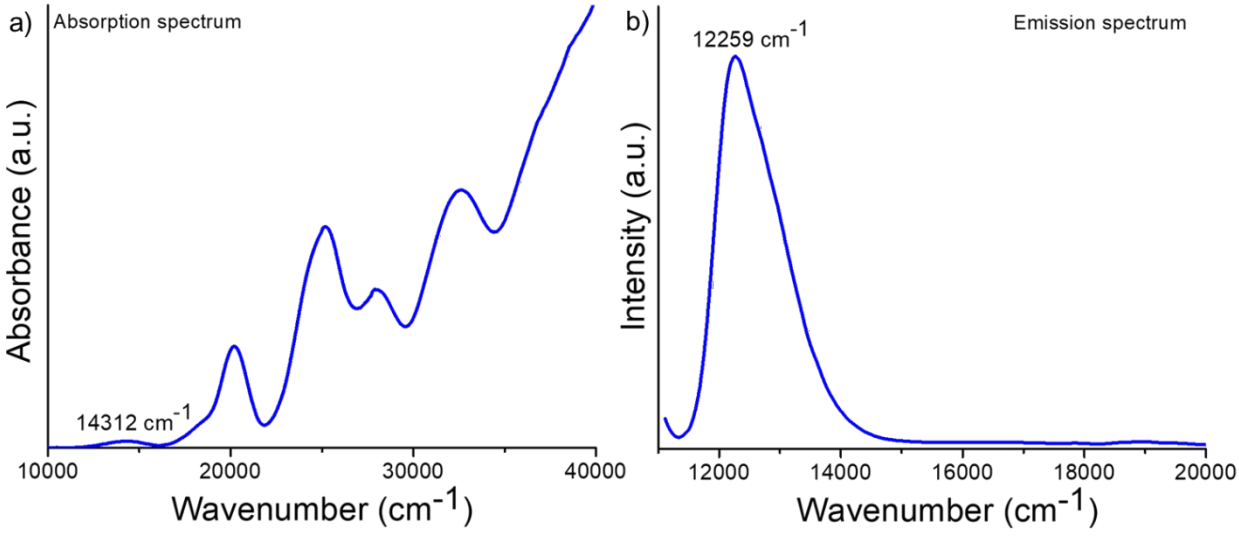

Figure S40. a) Absorption and b) emission spectra of Ag_{21} in energy scale. The apparent stokes shift of 2053 cm^{-1} was calculated from the energy difference between the absorption edge and emission maximum.

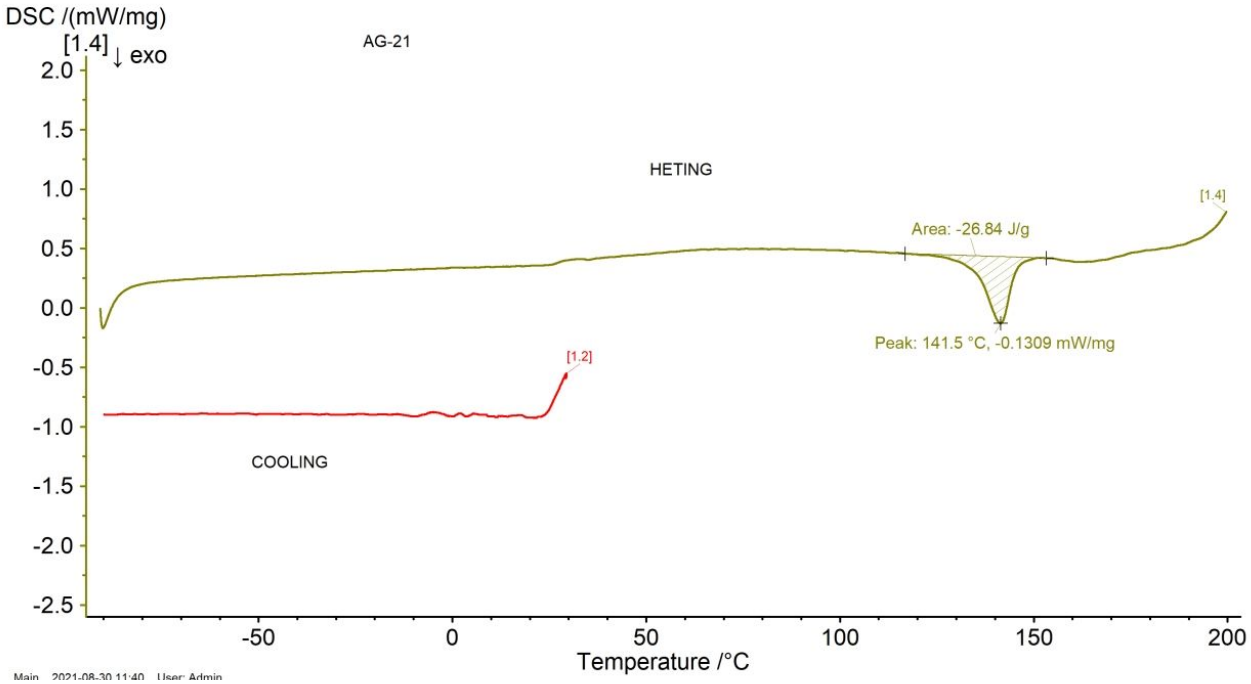

Figure S41. Differential scanning calorimetry (DSC) data of Ag_{21} microcrystals. Data was collected in a cooling curve from room temperature (25 °C) to -90 °C followed by a heating curve from -90 to 200 °C. The first exothermic peak at 141.5 °C indicates a structural rearrangement of the cluster.

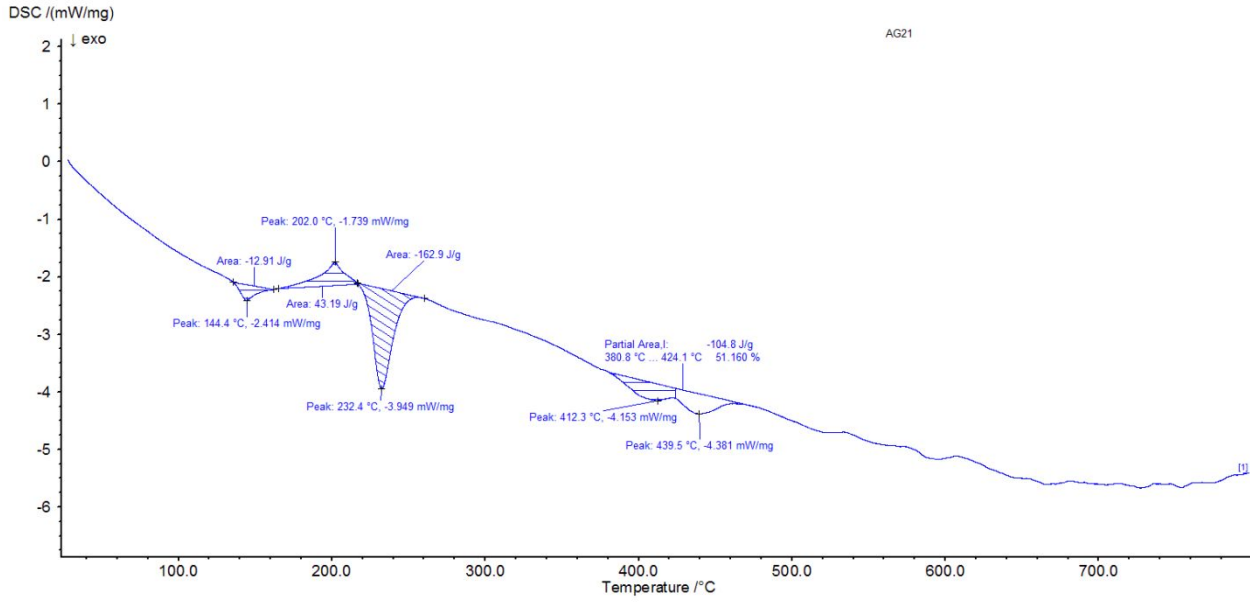

Figure S42. Differential scanning calorimetry (DSC) data of Ag_{21} microcrystals for the heating curve from 25 to 800 °C.

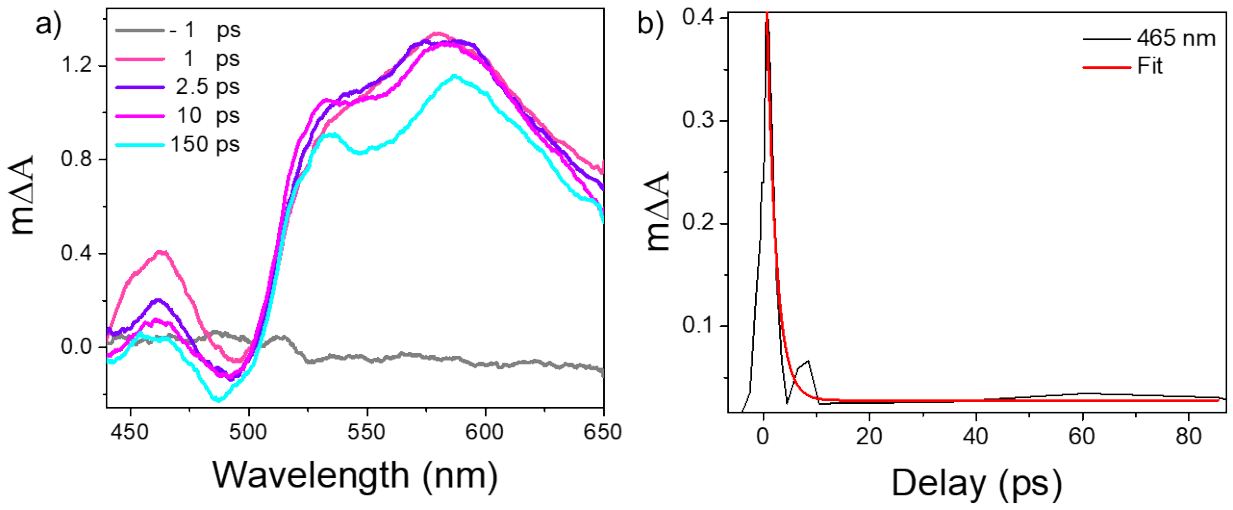

Figure S43. (a) Spectral slices of the TA at the selected time scales, showing fast decay profile of ESA at 465 nm. (b) Temporal evolution of 465 nm ESA features, where it decays in the early time scale.

4. References

(1) Bootharaju, M. S.; Dey, R.; Gevers, L. E.; Hedhili, M. N.; Basset, J. M.; Bakr, O. M. A New Class of Atomically Precise, Hydride-Rich Silver Nanoclusters Co-Protected by Phosphines. *J. Am. Chem. Soc.* **2016**, *138*, 13770–13773.

(2) Ghosh, A.; Bodiuzzaman, M.; Nag, A.; Jash, M.; Baksi, A.; Pradeep, T. Sequential Dihydrogen Desorption from Hydride-Protected Atomically Precise Silver Clusters and the Formation of Naked Clusters in the Gas Phase. *ACS Nano* **2017**, *11*, 11145–11151.

(3) Enkovaara, J.; Rostgaard, C.; Mortensen, J. J.; Chen, J.; Dułak, M.; Ferrighi, L.; Gavnholt, J.; Glinsvad, C.; Haikola, V.; Hansen, H. A.; Kristoffersen, H. H.; Kuisma, M.; Larsen, A. H.; Lehtovaara, L.; Ljungberg, M.; Lopez-Acevedo, O.; Moses, P. G.; Ojanen, J.; Olsen, T.; Petzold, V.; Romero, N. A.; Stausholm-Møller, J.; Strange, M.; Tritsaris, G. A.; Vanin, M.; Walter, M.; Hammer, B.; Häkkinen, H.; Madsen, G. K. H.; Nieminen, R. M.; Nørskov, J. K.; Puska, M.; Rantala, T. T.; Schiøtz, J.; Thygesen, K. S.; Jacobsen, K. W. Electronic Structure Calculations with GPAW: A Real-Space Implementation of the Projector Augmented-Wave Method. *J. Phys. Condens. Matter* **2010**, *22* (253202), 1–24.

(4) Mortensen, J. J.; Hansen, L. B.; Jacobsen, K. W. Real-Space Grid Implementation of the Projector Augmented Wave Method. *Phys. Rev. B - Condens. Matter Mater. Phys.* **2005**, *71* (035109), 1–11.

(5) Perdew, J. P.; Burke, K.; Ernzerhof, M. Generalized Gradient Approximation Made Simple. *Phys. Rev. Lett.* **1996**, *77* (18), 3865–3868.